New State Transition Matrices for Relative Motion of Spacecraft Formations in Perturbed Orbits

Adam W. Koenig*

Aeronautics and Astronautics, Stanford University, Stanford, California, 94305, USA

Tommaso Guffanti†

Department of Aerospace Science and Technology, Politecnico di Milano, 20156, Milan, Italy

Simone D'Amico‡

Aeronautics and Astronautics, Stanford University, Stanford, California, 94305, USA

This paper presents new state transition matrices that model the relative motion of two spacecraft in arbitrarily eccentric orbits perturbed by J_2 and differential drag for three state definitions based on relative orbital elements. These matrices are derived by first performing a Taylor expansion on the equations of relative motion including all considered perturbations and subsequently computing an exact, closed-form solution of the resulting linear differential equations. Both density-model-specific and density-model-free differential drag formulations are included. Density-model-specific formulations require a-priori knowledge of the atmosphere, while density-model-free formulations remove this requirement by augmenting the relative state with a set of parameters which are estimated in flight. The resulting state transition matrices are used to generalize the geometric interpretation of the effects of J_2 and differential drag on relative motion in near-circular orbits provided in previous works to arbitrarily eccentric orbits. Additionally, this paper harmonizes current literature by demonstrating that a number of state transition matrices derived by previous authors using various techniques can be found by subjecting the models presented in this paper to more restrictive assumptions. Finally, the presented state transition matrices are validated through comparison with a high-fidelity numerical orbit propagator. It is found that the models including density-model-free differential drag exhibit much better performance than their density-model-specific counterparts. Specifically, these state transition matrices are able to reduce propagation errors by at least an order-of-magnitude when compared to models including only J_2 and are able to match or exceed the accuracy of comparable models in literature over a broad range of orbit scenarios.

I. Introduction

This paper addresses modeling of the relative motion of two spacecraft in earth orbit in order to serve the needs of future formation-flying missions. To date, the majority of formation-flying missions such as GRACE,[1] TanDEM-X,[2] and PRISMA[3] have flown in low earth orbit. However, NASA's recently launched Magnetospheric Multiscale (MMS) mission includes a formation of four satellites in elliptical orbits.[4] Furthermore, a number of proposed missions including ESA's PROBA-3,[5] the Space Rendezvous Laboratory's (SLAB) Miniaturized Distributed Occulter/Telescope (mDOT),[6] and others[7] will operate with increased autonomy in more diverse scenarios using smaller spacecraft buses. Indeed, these missions call for guidance,

*Ph.D. Candidate, Aeronautics and Astronautics, Stanford University, 496 Lomita Mall, Stanford, CA 94305, AIAA Student Member.

†M. S. Graduate, Department of Aerospace Science and Technology, Politecnico di Milano, via La Masa 34, 20156, Milan, Italy

‡Assistant Professor, Aeronautics and Astronautics, Stanford University, 496 Lomita Mall, Stanford, CA 94305, AIAA Member.

navigation, and control (GN&C) systems capable of meeting stricter requirements than those currently flying with reduced computational resources. To meet these needs, new dynamic models are required that are more accurate, computationally efficient, and are valid for a wider range of applications than those currently available in literature.

State transition matrices (STMs) have been employed extensively to model the relative motion of spacecraft formations because of their computational efficiency. A comprehensive survey of STMs and other relative motion models available in literature can be found in a recent work by Sullivan et al.[8] and a summary of key STM developments is included in the following. The first STM for spacecraft relative motion is the well-known Hill-Clohessy-Wiltshire (HCW) STM for formations in unperturbed, near-circular orbits.[9] The HCW STM uses a relative state defined from the relative position and velocity in a rotating frame centered about one of the spacecraft. This STM has flight heritage on numerous programs including Gemini, Apollo, the Space Shuttle, and many others.[10–12] While the initial HCW model employed rectilinear relative position and velocity, other authors have found that an identical STM can be used to propagate a relative state defined through curvilinear coordinates with orders-of-magnitude better accuracy.[13] Taking a slightly different approach, Lovell and Tragesser used nonlinear combinations of the relative position and velocity to define a state based on the HCW invariants.[14] Additionally, works by Schweighart and Izzo expand on the HCW model by including first-order secular effects of J_2 and differential drag.[15,16] However, all of these models are only valid for near-circular orbits. As of now the Yamanaka-Ankersen STM,[17] which includes no perturbations, is widely considered to be the state-of-the-art solution for linear propagation of relative position and velocity in eccentric orbits and will be incorporated in the GN&C system of the PROBA-3 solar coronagraph mission.[18]

More recent works have derived STMs using states defined as functions of the Keplerian orbit elements of the spacecraft, hereafter called relative orbital elements (ROE). These states vary slowly with time and allow astrodynamics tools such as the Gauss variational equations[19] to be leveraged to include perturbations. Noteworthy contributions can be divided into two general tracks. The first track originates from an STM derived by Gim and Alfriend which includes first-order secular and osculating J_2 effects in arbitrarily eccentric orbits.[20] This STM was used in the design process for NASA's MMS mission[21] and is employed in the maneuver-planning algorithm of NASA's CPOD mission.[22] A similar STM was later derived for a fully nonsingular ROE state[23] and more recent works have expanded this approach to include higher-order zonal geopotential harmonics.[24] However, this approach has not yet produced an STM including non-conservative perturbations. Meanwhile, researchers at SLAB and collaborators have worked independently to develop models using a different ROE state. Specifically, D'Amico derived an STM which captures the first-order secular effects of J_2 on formations in near-circular orbits[25] in his thesis. This model has since been expanded to include the effect of differential drag on the relative semi-major axis,[26] and the effect of time-varying differential drag on the relative eccentricity vector.[27] This state formulation was first used in flight to plan the GRACE formation's longitude swap maneuver[28] and has since found application in the GN&C systems of the TanDEM-X[29] and PRISMA[3] missions as well as the planned AVANTI experiment.[30] However, to date neither of these approaches has produced an STM including both J_2 and differential drag in eccentric orbits. Such an STM could find immediate application on proposed formation-flying missions such as mDOT.

In order to meet this need, the contributions of this paper to the state-of-the-art are as follows:

1. Modeling of differential drag is expanded. First, a closed-form, density-model-specific (DMS) approximation of the secular effects of differential drag on formations in eccentric orbits is fit to data from a set of simulations using the Harris-Priester atmospheric density model. In order to accommodate uncertainty in atmospheric density knowledge, a density-model-free (DMF) formulation of the effects of differential drag on eccentric orbits is derived from the fundamental assumption that atmospheric drag causes eccentric orbits to circularize. This model requires the ROE to be augmented with an a-priori estimate of the time derivative of the relative semi-major axis, which can be estimated in flight. Additionally, a generalized DMF differential drag model for orbits of arbitrary eccentricity is developed using approach inspired by Gaias' model of time-varying differential drag in near-circular orbits.[27]

2. STMs for three mean ROE state definitions are derived using a simple, two-step method that allows inclusion of multiple perturbations in orbits of arbitrary eccentricity. First, a Taylor expansion is performed on the equations of relative motion including all considered perturbations. Next, an exact, closed-form solution of the resulting linear differential equations is computed. Four STMs are derived

for each ROE state. These include one STM which includes only the J_2 perturbation and three that include J_2 and one of the aforementioned differential drag models.

3. The STMs are exploited to generalize the geometric interpretation of the effects of J_2 and differential drag on relative motion in near-circular orbits provided by D'Amico[25] to orbits of arbitrary eccentricity.

4. Current literature on STMs including first-order secular effects of J_2 and differential drag is harmonized. Specifically, it is demonstrated that several of the STMs published by different authors under different derivation assumptions can be found by subjecting the STMs derived in this paper to more restrictive assumptions.

5. The STMs are validated through comparison with a high-fidelity numerical orbit propagator including a general set of perturbations. In order to assess the robustness of the DMF differential drag models, an initialization procedure is employed which includes estimation errors consistent with the real-time estimation uncertainty of current state-of-the-art relative navigation systems. It is found that STMs including DMF differential drag models exhibit much better propagation accuracy than their DMS counterparts. Additionally, the STMs including the DMF differential drag model for orbits of arbitrary eccentricity are able to match or exceed the accuracy of comparable models in literature in a broad range of orbit scenarios.

After this introduction, the ROE states are defined in Sec. II and the derivation method is described in Sec. III. An STM that models the effects of Keplerian relative motion on the described state definitions is derived in Sec. IV. This STM is generalized to include the secular effects of J_2 on each of the ROE states in Sec. V. The resulting J_2 STMs are further expanded to include a DMS differential drag model for eccentric orbits derived from a closed-form approximation of the Harris-Priester atmospheric density model in Sec. VI. In order to address the known uncertainty in atmospheric density models, the J_2 STMs are generalized to include the DMF differential drag model for eccentric orbits in Sec. VII. The DMF drag model is generalized to orbits of arbitrary eccentricity in Sec. VIII. The range of validity for these STMs is found through analysis of perturbations affecting relative motion in earth orbit in Sec. IX. Finally, these STMs are validated by comparison with a high-fidelity numerical orbit propagator in Sec. X.

II. State Definitions

This paper presents STMs for three states including singular, denoted by subscript s, quasi-nonsingular, denoted by subscript qns, and nonsingingular, denoted by subscript ns, ROE. Let a, e, i, Ω, ω, and M denote the classical Keplerian orbit elements. For a formation consisting of two spacecraft including a chief, denoted by subscript c, and a deputy, denoted by subscript d, the singular ROE, $\delta\boldsymbol{\alpha}_s$, are defined as

$$\delta\boldsymbol{\alpha}_s = \begin{pmatrix} \delta a \\ \delta M \\ \delta e \\ \delta\omega \\ \delta i \\ \delta\Omega \end{pmatrix} = \begin{pmatrix} (a_d - a_c)/a_c \\ M_d - M_c \\ e_d - e_c \\ \omega_d - \omega_c \\ i_d - i_c \\ \Omega_d - \Omega_c \end{pmatrix}, \tag{1}$$

the quasi-nonsingular ROE, $\delta\boldsymbol{\alpha}_{qns}$, are defined as

$$\delta\boldsymbol{\alpha}_{qns} = \begin{pmatrix} \delta a \\ \delta\lambda \\ \delta e_x \\ \delta e_y \\ \delta i_x \\ \delta i_y \end{pmatrix} = \begin{pmatrix} (a_d - a_c)/a_c \\ (M_d + \omega_d) - (M_c + \omega_c) + (\Omega_d - \Omega_c)\cos(i_c) \\ e_d\cos(\omega_d) - e_c\cos(\omega_c) \\ e_d\sin(\omega_d) - e_c\sin(\omega_c) \\ i_d - i_c \\ (\Omega_d - \Omega_c)\sin(i_c) \end{pmatrix}, \tag{2}$$

and the nonsingular ROE, $\delta\boldsymbol{\alpha}_{ns}$, are defined as

$$\delta\boldsymbol{\alpha}_{ns} = \begin{pmatrix} \delta a \\ \delta l \\ \delta e_x^* \\ \delta e_y^* \\ \delta i_x^* \\ \delta i_y^* \end{pmatrix} = \begin{pmatrix} (a_d - a_c)/a_c \\ (M_d + \omega_d + \Omega_d) - (M_c + \omega_c + \Omega_c) \\ e_d \cos(\omega_d + \Omega_d) - e_c \cos(\omega_c + \Omega_c) \\ e_d \sin(\omega_d + \Omega_d) - e_c \sin(\omega_c + \Omega_c) \\ \tan(i_d/2)\cos(\Omega_d) - \tan(i_c/2)\cos(\Omega_c) \\ \tan(i_d/2)\sin(\Omega_d) - \tan(i_c/2)\sin(\Omega_c) \end{pmatrix}. \tag{3}$$

The singular state is so named because it is not uniquely defined when either spacecraft is in a circular or equatorial orbit. Similarly, the quasi-nonsingular state is not unique when the deputy is in an equatorial orbit. The nonsingular state is uniquely defined for all possible chief and deputy orbits.

These state definitions are similar to those used by other authors in literature. The singular state is nearly identical to the orbit element differences employed by Schaub.[31] The only difference in this definition is that the semi-major axis difference is normalized by a_c in order to keep all of the terms dimensionless. The quasi-nonsingular state is identical to D'Amico's ROE,[25] which offer several advantageous properties. First, the state components match the integration constants of the HCW equations for near-circular orbits and the Tschauner-Hempel equations for eccentric orbits.[32] Additionally, they provide insight into passive safety and stability for formation-flying design in a simple manner using eccentricity/inclination vector separation.[33] This state is also similar to that used by Gim and Alfriend in the derivation of their J_2-perturbed STM[20] except that Gim's state definition uses the true anomaly in place of the mean anomaly. Finally, the nonsingular state is also equivalent to the differential equinoctial elements employed by Gim and Alfriend[23] except for the use of the mean anomaly. The mean anomaly is preferred for this application because $M_d - M_c$ is constant for unperturbed orbits of equal energy regardless of eccentricity.

III. Derivation Methodology

The STMs presented in this paper are all derived using a simple method which allows inclusion of multiple perturbations in orbits of arbitrary eccentricity and admits a wide range of ROE states. The only requirement is a closed-form expression of the time derivatives of the relative state as a function of the absolute states of the chief and deputy. Consider a general absolute state $\boldsymbol{\alpha}$ and relative state $\delta\boldsymbol{\alpha}$ which include parameters to model nonconservative forces (e.g. ballistic coefficients with respect to atmospheric drag or solar radiation pressure). Let the time derivatives of the relative state be given as

$$\delta\dot{\boldsymbol{\alpha}}(t) = \mathbf{f}(\boldsymbol{\alpha}_d(\boldsymbol{\alpha}_c(t), \delta\boldsymbol{\alpha}(t)), \boldsymbol{\alpha}_c(t), \boldsymbol{\gamma}) \tag{4}$$

where the absolute state of the deputy is formulated explicitly as a function of the chief state and the relative state and $\boldsymbol{\gamma}$ denotes a general set of parameters relevant to included perturbations (e.g the pointing vector to the sun, current atmospheric data, third-body ephemerides). The STMs are derived by first performing a first-order Taylor expansion on the equations of relative motion, given as

$$\delta\dot{\boldsymbol{\alpha}}(t) = \mathbf{A}(\boldsymbol{\alpha}_c(t), \boldsymbol{\gamma})\delta\boldsymbol{\alpha}(t) + \mathcal{O}(\delta\alpha^2) \qquad \mathbf{A}(\boldsymbol{\alpha}_c(t), \boldsymbol{\gamma}) = \left.\frac{\partial\delta\dot{\boldsymbol{\alpha}}}{\partial\boldsymbol{\alpha}_d}\right|_{\delta\boldsymbol{\alpha}=0} \left.\frac{\partial\boldsymbol{\alpha}_d}{\partial\delta\boldsymbol{\alpha}}\right|_{\boldsymbol{\alpha}_d=\boldsymbol{\alpha}_c} \tag{5}$$

where the plant matrix $\mathbf{A}$ is computed by a simple chain rule derivative. If the terms of $\mathbf{A}$ are constant, the resulting system of linear differential equations is solved exactly in closed-form, given as

$$\delta\boldsymbol{\alpha}(t_i + \tau) = \boldsymbol{\Phi}(\boldsymbol{\alpha}_c(t_i), \boldsymbol{\gamma}, \tau)\delta\boldsymbol{\alpha}(t_i) \tag{6}$$

where $\boldsymbol{\Phi}(\boldsymbol{\alpha}_c(t_i), \boldsymbol{\gamma}, \tau)$ denotes the STM. However, in some cases the plant matrix cannot reasonably be treated as time-invariant. This issue is corrected by transforming the state into a modified form by a simple linear transformation provided that the relevant dynamics of the chief absolute state are known. The STM for the modified state can then be computed from the time-invariant plant matrix. In these cases, the STM for the original state can be expressed in closed-form as

$$\boldsymbol{\Phi}(\boldsymbol{\alpha}_c(t_i), \boldsymbol{\gamma}, \tau) = \mathbf{J}^{-1}(\boldsymbol{\alpha}_c(t_i) + \dot{\boldsymbol{\alpha}}_c(t_i)\tau)\boldsymbol{\Phi}'(\boldsymbol{\alpha}_c(t_i), \boldsymbol{\gamma}, \tau)\mathbf{J}(\boldsymbol{\alpha}_c(t_i)). \tag{7}$$

where $\dot{\boldsymbol{\alpha}}_c(t_i)$ denotes the time derivative of the chief state at time t_i, $\boldsymbol{\Phi}'(\boldsymbol{\alpha}_c(t_i), \boldsymbol{\gamma}, \tau)$ denotes the STM for the modified state, and $\mathbf{J}(\boldsymbol{\alpha}_c(t))$ denotes the transformation matrix to the modified state at time t.

IV. Keplerian Dynamics

Under the assumption of a Keplerian orbit, the time derivatives of the orbit elements are given as

$$\dot{a} = \dot{e} = \dot{i} = \dot{\omega} = \dot{\Omega} = 0 \qquad \dot{M} = n = \frac{\sqrt{\mu}}{a^{3/2}} \tag{8}$$

Because only M is time varying, the time derivatives of all previously described ROE states are equivalent and given as

$$\delta\dot{\boldsymbol{\alpha}} = \begin{pmatrix} 0 \\ \dot{M}_d - \dot{M}_c \\ 0 \\ 0 \\ 0 \\ 0 \end{pmatrix} = \sqrt{\mu} \begin{pmatrix} 0 \\ a_d^{-3/2} - a_c^{-3/2} \\ 0 \\ 0 \\ 0 \\ 0 \end{pmatrix}. \tag{9}$$

The first-order Taylor expansion of Eq. 9 about zero separation is given as

$$\delta\dot{\boldsymbol{\alpha}} = \mathbf{A}^{kep}(\boldsymbol{\alpha}_c)\delta\boldsymbol{\alpha} + \mathcal{O}(\delta\alpha^2) \qquad \mathbf{A}^{kep}(\boldsymbol{\alpha}_c) = \left[\begin{array}{c:c} 0 & \mathbf{0}^{2\times5} \\ -1.5n & \\ \hdashline \mathbf{0}^{4\times1} & \mathbf{0}^{4\times5} \end{array}\right]. \tag{10}$$

Because the along-track separation terms depend only on the constant δa, the corresponding STM for Keplerian relative motion, $\boldsymbol{\Phi}^{kep}(\boldsymbol{\alpha}_c(t_i), \tau)$, is given as

$$\boldsymbol{\Phi}^{kep}(\boldsymbol{\alpha}_c(t_i), \tau) = \mathbf{I} + \mathbf{A}^{kep}(\boldsymbol{\alpha}_c(t_i))\tau. \tag{11}$$

The range of applicability of this model can be assessed by determining which of the higher-order terms in the Taylor expansion given in Eq. 10 are non-zero. It is evident from Eq. 9 that Keplerian relative motion depends only on the semi-major axes of each of the spacecraft orbits. Accordingly, the only non-zero higher-order terms will be proportional to powers of δa. Thus, this relative motion model is valid for unperturbed orbits with small δa and arbitrary separation in all other state components.

V. Inclusion of the J_2 Perturbation

The Keplerian STM is generalized to include the first-order secular effects of the second-order zonal geopotential harmonic, J_2, for each of the previously described states in the following. The individual terms of these J_2 STMs are included in Appendix A. The J_2 perturbation causes secular drifts in the mean anomaly, right ascension of the ascending node (RAAN), and the argument of perigee. These drift rates are given by Brouwer[34] as

$$\begin{pmatrix} \dot{M} \\ \dot{\omega} \\ \dot{\Omega} \end{pmatrix} = \frac{3}{4}\frac{J_2 R_E^2 \sqrt{\mu}}{a^{7/2}\eta^4} \begin{pmatrix} \eta(3\cos^2(i) - 1) \\ 5\cos^2(i) - 1 \\ -2\cos(i) \end{pmatrix}. \tag{12}$$

The following substitutions are employed to simplify the following derivations.

$$\eta = \sqrt{1 - e^2} \qquad \kappa = \frac{3}{4}\frac{J_2 R_E^2 \sqrt{\mu}}{a^{7/2}\eta^4} \qquad E = 1 + \eta \qquad F = 4 + 3\eta \qquad G = \frac{1}{\eta^2} \tag{13}$$

$$P = 3\cos^2(i) - 1 \qquad Q = 5\cos^2(i) - 1 \qquad R = \cos(i) \qquad S = \sin(2i) \qquad T = \sin^2(i) \tag{14}$$

$$U = \sin(i) \qquad V = \tan(i/2) \qquad W = \cos^2(i/2) \tag{15}$$

V.A. Singular State Derivation

The time derivatives of the singular ROE due to J_2 are computed by differentiating Eq. 1 with respect to time and substituting in the drift rates given in Eq. 12, yielding

$$\delta\dot{\boldsymbol{\alpha}}_s = \kappa_d \begin{pmatrix} 0 \\ \eta_d(3\cos^2(i_d)-1) \\ 0 \\ 5\cos^2(i_d)-1 \\ 0 \\ -2\cos(i_d) \end{pmatrix} - \kappa_c \begin{pmatrix} 0 \\ \eta_c(3\cos^2(i_c)-1) \\ 0 \\ 5\cos^2(i_c)-1 \\ 0 \\ -2\cos(i_c) \end{pmatrix}. \tag{16}$$

The first-order Taylor expansion of Eq. 16 about zero separation is given as

$$\delta\dot{\boldsymbol{\alpha}}_s = \mathbf{A}_s^{J_2}(\boldsymbol{\alpha}_c)\delta\boldsymbol{\alpha}_s + \mathcal{O}(\delta\alpha_s^2) \qquad \mathbf{A}_s^{J_2}(\boldsymbol{\alpha}_c) = \kappa \begin{bmatrix} 0 & 0 & 0 & 0 & 0 & 0 \\ -\frac{7}{2}\eta P & 0 & 3e\eta GP & 0 & -3\eta S & 0 \\ 0 & 0 & 0 & 0 & 0 & 0 \\ -\frac{7}{2}Q & 0 & 4eGQ & 0 & -5S & 0 \\ 0 & 0 & 0 & 0 & 0 & 0 \\ 7R & 0 & -8eGR & 0 & 2U & 0 \end{bmatrix}. \tag{17}$$

This plant matrix exhibits two useful properties. First, δa, δe, and δi are all constant. Second, the time derivatives of δM, $\delta\omega$, and $\delta\Omega$ depend only on these constant terms. Because of these properties, the J_2 STM for the singular state, $\boldsymbol{\Phi}_s^{J_2}(\boldsymbol{\alpha}_c(t_i),\tau)$, is simply expressed as

$$\boldsymbol{\Phi}_s^{J_2}(\boldsymbol{\alpha}_c(t_i),\tau) = \mathbf{I} + (\mathbf{A}^{kep}(\boldsymbol{\alpha}_c(t_i)) + \mathbf{A}_s^{J_2}(\boldsymbol{\alpha}_c(t_i)))\tau. \tag{18}$$

The range of applicability of this model can be assessed by again considering higher-order terms of the Taylor expansion. It is evident from Eq. 16 that the time derivatives of the state elements do not depend on Ω, ω, or M. Accordingly, all partial derivatives of any order with respect to $\delta\Omega$, $\delta\omega$, and δM are zero. However, all second-order partial derivatives with respect to the remaining state elements are non-zero. It follows that this model is valid for small separations in δa, δe, and δi, but arbitrarily large separation in $\delta\Omega$, $\delta\omega$, and δM.

V.B. Quasi-Nonsingular State Derivation

It is clear by inspection of the quasi-nonsingular state definition in Eq. 2 that the associated plant matrix will not have the advantageous sparsity of the singular plant matrix due to the coupling between the eccentricity and the argument of perigee. However, this problem can be corrected by considering a modified form of the quasi-nonsingular state, $\delta\boldsymbol{\alpha}_{qns'}$, obtained by the following linear transformation

$$\delta\boldsymbol{\alpha}_{qns'} = \mathbf{J}_{qns}(\boldsymbol{\alpha}_c)\delta\boldsymbol{\alpha}_{qns} \qquad \mathbf{J}_{qns}(\boldsymbol{\alpha}_c) = \left[\begin{array}{c:cc:c} \mathbf{I}^{2\times2} & \mathbf{0}^{2\times2} & & \mathbf{0}^{2\times2} \\ \hdashline \mathbf{0}^{2\times2} & \cos(\omega) & \sin(\omega) & \mathbf{0}^{2\times2} \\ & -\sin(\omega) & \cos(\omega) & \\ \hdashline \mathbf{0}^{2\times2} & \mathbf{0}^{2\times2} & & \mathbf{I}^{2\times2} \end{array}\right] \tag{19}$$

which is a simple rotation of the relative eccentricity vector. These modified quasi-nonsingular ROE are given as

$$\delta\boldsymbol{\alpha}_{qns'} = \begin{pmatrix} \delta a \\ \delta\lambda \\ \delta e'_x \\ \delta e'_y \\ \delta i_x \\ \delta i_y \end{pmatrix} = \begin{pmatrix} (a_d - a_c)/a_c \\ (M_d - M_c) + (\omega_d - \omega_c) + (\Omega_d - \Omega_c)\cos i_c \\ e_d\cos(\omega_d - \omega_c) - e_c \\ e_d\sin(\omega_d - \omega_c) \\ i_d - i_c \\ (\Omega_d - \Omega_c)\sin i_c \end{pmatrix}. \tag{20}$$

The key benefit of this state definition is found by considering the partial derivatives of the deputy orbit elements with respect to the relative state components evaluated at zero separation, which are given as

$$\frac{\partial e_d}{\partial \delta e'_x} = 1 \qquad \frac{\partial e_d}{\partial \delta e'_y} = 0 \qquad \frac{\partial \omega_d}{\partial \delta e'_x} = 0 \qquad \frac{\partial \omega_d}{\partial \delta e'_y} = \frac{1}{e}. \tag{21}$$

From these partial derivatives it is evident that to first order $\delta e'_x$ and δe are equivalent and the effects of changes in eccentricity and argument of perigee on the relative eccentricity vector are decoupled. The time derivatives of $\delta\boldsymbol{\alpha}_{qns'}$ due to J_2 are computed by the same method used for the singular state and are given as

$$\delta\dot{\boldsymbol{\alpha}}_{qns'} = \kappa_d \begin{pmatrix} 0 \\ \eta_d(3\cos^2(i_d)-1) + (5\cos^2(i_d)-1) - 2\cos(i_d)\cos(i_c) \\ -e_d \sin(\omega_d - \omega_c)(5\cos^2(i_d)-1) \\ e_d \cos(\omega_d - \omega_c)(5\cos^2(i_d)-1) \\ 0 \\ -2\cos(i_d)\sin(i_c) \end{pmatrix} - \kappa_c \begin{pmatrix} 0 \\ (1+\eta_c)(3\cos^2(i_c)-1) \\ -e_d \sin(\omega_d - \omega_c)(5\cos^2(i_c)-1) \\ e_d \cos(\omega_d - \omega_c)(5\cos^2(i_c)-1) \\ 0 \\ -2\cos(i_c)\sin(i_c) \end{pmatrix}. \tag{22}$$

The first-order Taylor expansion of Eq. 22 about zero separation is given as

$$\delta\dot{\boldsymbol{\alpha}}_{qns'} = \mathbf{A}^{J_2}_{qns'}(\boldsymbol{\alpha}_c)\delta\boldsymbol{\alpha}_{qns'} + \mathcal{O}(\delta\alpha^2_{qns'}) \qquad \mathbf{A}^{J_2}_{qns'}(\boldsymbol{\alpha}_c) = \kappa \begin{bmatrix} 0 & 0 & 0 & 0 & 0 & 0 \\ -\frac{7}{2}EP & 0 & eFGP & 0 & -FS & 0 \\ 0 & 0 & 0 & 0 & 0 & 0 \\ -\frac{7}{2}eQ & 0 & 4e^2GQ & 0 & -5eS & 0 \\ 0 & 0 & 0 & 0 & 0 & 0 \\ \frac{7}{2}S & 0 & -4eGS & 0 & 2T & 0 \end{bmatrix}. \tag{23}$$

This plant matrix has the same structure as that of the singular state. Thus, the STM can be constructed in the same way except that coordinate transformations to and from the modified state at the beginning and end of the propagation, respectively, are required. Thus, the J_2 STM for the quasi-nonsingular state, $\boldsymbol{\Phi}^{J_2}_{qns}(\boldsymbol{\alpha}_c(t_i),\tau)$, is given as

$$\boldsymbol{\Phi}^{J_2}_{qns}(\boldsymbol{\alpha}_c(t_i),\tau) = \mathbf{J}^{-1}_{qns}(\boldsymbol{\alpha}_c(t_i) + \dot{\boldsymbol{\alpha}}_c(t_i)\tau)(\mathbf{I} + (\mathbf{A}^{kep}(\boldsymbol{\alpha}_c(t_i)) + \mathbf{A}^{J_2}_{qns'}(\boldsymbol{\alpha}_c(t_i)))\tau)\mathbf{J}_{qns}(\boldsymbol{\alpha}_c(t_i)). \tag{24}$$

The range of applicability is again assessed by considering higher-order terms of the Taylor expansion. It is evident from Eq. 22 that the time derivative of the state does not depend on M or Ω, which correspond to the $\delta\lambda$ and δi_y state components. Accordingly, the model is valid for small separations in δa, δe_x, δe_y, and δi_x, but arbitrary separations in $\delta\lambda$ and δi_y. It follows that while the quasi-nonsingular state avoids the circular orbit singularity present in the singular state, the cost of this property is that arbitrary differences in the argument of perigee are no longer allowed.

V.C. Nonsingular State Derivation

The derivation procedure for the nonsingular state is identical to that of the quasi-nonsingular state. First, the nonsingular state is transformed into a modified form, $\delta\boldsymbol{\alpha}_{ns'}$, which recovers the advantageous sparsity of the plant matrix using the following linear transformation

$$\delta\boldsymbol{\alpha}_{ns'} = \mathbf{J}_{ns}(\boldsymbol{\alpha}_c)\delta\boldsymbol{\alpha}_{ns} \qquad \mathbf{J}_{ns}(\boldsymbol{\alpha}_c) = \left[\begin{array}{c|cc|cc} \mathbf{I}^{2\times2} & \multicolumn{2}{c|}{\mathbf{0}^{2\times2}} & \multicolumn{2}{c}{\mathbf{0}^{2\times2}} \\ \hline \mathbf{0}^{2\times2} & \cos(\omega+\Omega) & \sin(\omega+\Omega) & \multicolumn{2}{c}{\multirow{2}{*}{$\mathbf{0}^{2\times2}$}} \\ & -\sin(\omega+\Omega) & \cos(\omega+\Omega) & & \\ \hline \mathbf{0}^{2\times2} & \multicolumn{2}{c|}{\mathbf{0}^{2\times2}} & \cos(\Omega) & \sin(\Omega) \\ & & & -\sin(\Omega) & \cos(\Omega) \end{array}\right] \tag{25}$$

which consists of simple rotations of the relative eccentricity and inclination vectors. These modified nonsingular ROE are given as

$$\delta\boldsymbol{\alpha}_{ns'} = \begin{pmatrix} \delta a \\ \delta\lambda \\ \delta e_x'^* \\ \delta e_y'^* \\ \delta i_x'^* \\ \delta i_y'^* \end{pmatrix} = \begin{pmatrix} (a_d - a_c)/a_c \\ (M_d + \omega_d + \Omega_d) - (M_c + \omega_c + \Omega_c) \\ e_d \cos(\omega_d + \Omega_d - \omega_c - \Omega_c) - e_c \\ e_d \sin(\omega_d + \Omega_d - \omega_c - \Omega_c) \\ \tan(i_d/2)\cos(\Omega_d - \Omega_c) - \tan(i_c/2) \\ \tan(i_d/2)\sin(\Omega_d - \Omega_c) \end{pmatrix}. \tag{26}$$

The key advantage of this state again follows from the partial derivatives of the absolute state of the deputy with respect to the relative state components evaluated at zero separation, which are given as

$$\begin{aligned} \frac{\partial e_d}{\partial \delta e_x'^*} &= 1 \qquad \frac{\partial e_d}{\partial \delta e_y'^*} = 0 \qquad \frac{\partial \omega_d}{\partial \delta e_x'^*} = 0 \qquad \frac{\partial \omega_d}{\partial \delta e_y'^*} = \frac{1}{e} \\ \frac{\partial i_d}{\partial \delta i_x'^*} &= 2\cos^2(i/2) \qquad \frac{\partial i_d}{\partial \delta i_y'^*} = 0 \qquad \frac{\partial \Omega_d}{\partial \delta i_x'^*} = 0 \qquad \frac{\partial \Omega_d}{\partial \delta i_y'^*} = \cot(i/2). \end{aligned} \tag{27}$$

From these partial derivatives it is clear that to first order $\delta e_x'^*$ and δe are equivalent and the effects of changes in the deputy eccentricity and argument of perigee on the relative eccentricity vector are decoupled. Similarly, $\delta i_x'^*$ is proportional to δi and the effects of changes in the deputy inclination and RAAN on the relative inclination vector are decoupled. As before, the time derivatives of $\delta\boldsymbol{\alpha}_{ns'}$ due to J_2 are given as

$$\begin{aligned} \delta\dot{\boldsymbol{\alpha}}_{ns'} = \kappa_d &\begin{pmatrix} 0 \\ \eta_d(3\cos^2(i_d) - 1) + (5\cos^2(i_d) - 1) - 2\cos(i_d) \\ -e_d \sin(\omega_d + \Omega_d - \omega_c - \Omega_c)(5\cos^2(i_d) - 1 - 2\cos(i_d)) \\ e_d \cos(\omega_d + \Omega_d - \omega_c - \Omega_c)(5\cos^2(i_d) - 1 - 2\cos(i_d)) \\ 2\tan(i_d/2)\sin(\Omega_d - \Omega_c)\cos(i_d) \\ -2\tan(i_d/2)\cos(\Omega_d - \Omega_c)\cos(i_d) \end{pmatrix} \\ -\kappa_c &\begin{pmatrix} 0 \\ \eta_c(3\cos^2(i_c) - 1) + (5\cos^2(i_c) - 1) - 2\cos(i_c) \\ -e_d \sin(\omega_d + \Omega_d - \omega_c - \Omega_c)(5\cos^2(i_c) - 1 - 2\cos(i_c)) \\ e_d \cos(\omega_d + \Omega_d - \omega_c - \Omega_c)(5\cos^2(i_c) - 1 - 2\cos(i_c)) \\ 2\tan(i_d/2)\sin(\Omega_d - \Omega_c)\cos(i_c) \\ -2\tan(i_d/2)\cos(\Omega_d - \Omega_c)\cos(i_c) \end{pmatrix}. \end{aligned} \tag{28}$$

The first-order Taylor expansion of Eq. 28 about zero separation is given as

$$\delta\dot{\boldsymbol{\alpha}}_{ns'} = \mathbf{A}^{J_2}_{ns'}(\boldsymbol{\alpha}_c)\delta\boldsymbol{\alpha}_{ns'} + \mathcal{O}(\delta\alpha^2_{ns'})$$

$$\mathbf{A}^{J_2}_{ns'}(\boldsymbol{\alpha}_c) = \kappa \begin{bmatrix} 0 & 0 & 0 & 0 & 0 & 0 \\ -\frac{7}{2}(\eta P + Q - 2R) & 0 & eG(3\eta P + 4Q - 8R) & 0 & 2W(-(3\eta+5)S + 2U) & 0 \\ 0 & 0 & 0 & 0 & 0 & 0 \\ -\frac{7}{2}e(Q - 2R) & 0 & 4e^2 G(Q - 2R) & 0 & 2eW(-5S + 2U) & 0 \\ 0 & 0 & 0 & 0 & 0 & 0 \\ 7RV & 0 & -8eGRV & 0 & 4UVW & 0 \end{bmatrix} \tag{29}$$

Finally, the J_2 STM for the nonsingular state, $\boldsymbol{\Phi}^{J_2}_{ns}(\boldsymbol{\alpha}_c(t_i), \tau)$, is given as

$$\boldsymbol{\Phi}^{J_2}_{ns}(\boldsymbol{\alpha}_c(t_i), \tau) = \mathbf{J}^{-1}_{ns}(\boldsymbol{\alpha}_c(t_i) + \dot{\boldsymbol{\alpha}}_c(t_i)\tau)(\mathbf{I} + (\mathbf{A}^{kep}(\boldsymbol{\alpha}_c(t_i)) + \mathbf{A}^{J_2}_{ns'}(\boldsymbol{\alpha}_c(t_i)))\tau)\mathbf{J}_{ns}(\boldsymbol{\alpha}_c(t_i)). \tag{30}$$

As before, the range of validity is assessed by considering the higher-order terms of the Taylor expansion. Because the time derivatives in Eq. 28 do not depend on M, it is evident that all partial derivatives with respect to δl will be zero. Thus, the model is valid for arbitrary separation in δl and small separations in all other state components. It follows that while the nonsingular state avoids the equatorial singularity present in the other definitions, the cost of this property is that arbitrary differences in RAAN are no longer allowed.

V.D. Relative Motion Description

At this stage it is useful to consider the relative motion produced by the preceding STMs. The combined effects of Keplerian relative motion and J_2 are illustrated in Fig. 1 for the singular (left), quasi-nonsingular (center), and nonsingular (right) ROE where the dotted lines denote breakdowns of individual phenomena

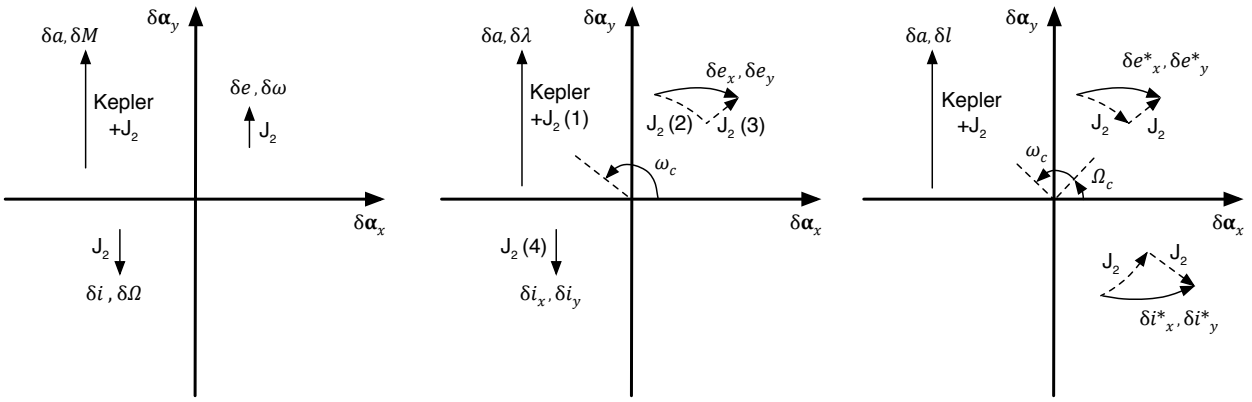

Figure 1. Combined effects of Keplerian relative motion and J_2 on singular (left), quasi-nonsingular (center), and nonsingular (right) ROE states. Dashed lines denote individual phenomena and solid lines denote combined trajectories.

and solid lines denote combined trajectories. First, consider the evolution of the quasi-nonsingular state. The combined effects of Kepler and J_2 produce four distinct types of motion as labeled in the figure: 1) a constant drift of $\delta\lambda$ due to both Keplerian relative motion and J_2, 2) a rotation of the relative eccentricity vector due to J_2, 3) a secular drift of the relative eccentricity vector proportional to the chief eccentricity and orthogonal to the phase angle of the chief argument of perigee due to J_2, and 4) a constant drift of δi_y due to J_2. The only difference between this model and D'Amico's model for near-circular orbits[25] is the constant drift of the relative eccentricity vector. The evolutions of the singular and nonsingular states can be interpreted as permutations of the evolution of the quasi-nonsingular state. Specifically, in the singular state δe remains constant while $\delta\omega$ exhibits a constant draft in the same way that δi_x is constant and δi_y drifts. Similarly, the relative inclination vector of the nonsingular state exhibits the same rotation and drift observed in the relative eccentricity vector of the quasi-nonsingular state.

It is noteworthy that the terms of the STMs for the quasi-nonsingular and nonsingular states are identical to those in the Gim-Alfriend STMs[20,23] for all state components except for the along track separation ($\delta\lambda$ and δl). The differing terms arise because the Gim-Alfriend STMs include the true anomaly in the state definition while this paper includes the mean anomaly.

VI. Inclusion of Density-Model-Specific Differential Drag in Eccentric Orbits

It is known that the primary effect of atmospheric drag on an eccentric orbit is a constant decay of the apogee radius while the perigee radius remains constant.[35] This phenomenon is captured by a dynamic model of the form

$$\dot{e} = g(\boldsymbol{\alpha}_c, \boldsymbol{\gamma}) \qquad \dot{a} = g(\boldsymbol{\alpha}_c, \boldsymbol{\gamma})\frac{a}{1-e} \tag{31}$$

where the factor $a/(1-e)$ in the time derivative of the semi-major axis ensures that the perigee radius is constant. The function g depends on the chief orbit, ballistic properties of the spacecraft, and parameters affecting atmospheric density such as the position of the sun and current solar activity levels. Indeed, it is well known that atmospheric models are characterized by high uncertainty. As such, the objective of the analysis in this section is not to present a definitive model of relative motion subject to differential drag, but is instead to present a method of generalizing the previously derived J_2 STMs to include the effects of differential drag using a-priori knowledge of the atmosphere. These DMS STMs are derived using a closed-form, differentiable dynamic model fit to data from a set of simulations using the Harris-Priester atmospheric density model[36] as a case study. However, the described method can be applied to any atmosphere model provided that the appropriate partial derivatives can be computed.

VI.A. A Closed-Form Dynamic Model for Atmospheric Drag

In order to develop a closed-form dynamic model for atmospheric drag it is first necessary to model the perturbing acceleration. The acceleration of a spacecraft due to atmospheric drag is modeled as

$$g_{drag} = -\frac{1}{2}\rho||\mathbf{v} - \mathbf{v}_{atm}||^2 B \tag{32}$$

where ρ denotes the atmospheric density, $\mathbf{v}$ denotes the velocity of the spacecraft in the earth-centered inertial (ECI) frame, $\mathbf{v}_{atm}$ denotes the velocity of the local atmosphere, and B denotes the ballistic coefficient of the spacecraft which is defined as

$$B = \frac{C_D S}{m} \tag{33}$$

where m is the spacecraft mass, S is the spacecraft cross-section area and C_D is the drag coefficient, which is a function of the spacecraft shape. From this model it is clear that the dynamics should vary linearly with the ballistic coefficient of the spacecraft. Furthermore, in eccentric orbits the effect of drag is only significant in a small region near the perigee, so it is reasonable to expect that the dynamics scale with the density at the perigee. Finally, the orbit shape must be considered. Specifically, for a given perigee height orbits with lower eccentricity will be more affected by atmospheric drag because the spacecraft spends more time in the lower atmosphere. With these considerations in mind, the authors performed a large number of orbit simulations using the Harris-Priester density model and fit a model of the form

$$\dot{a} = \frac{aB\rho_p f}{1-e} \qquad \dot{e} = B\rho_p f \qquad f = xe^y + z \tag{34}$$

to the data. In this model ρ_p denotes the atmospheric density at the orbit perigee and f is a function of the orbit eccentricity and empirical constants x, y, and z which captures the behavior of the atmospheric density in the vicinity of the perigee. The values of these empirical constants computed from a simple regression fit are

$$x = 1.61 \times 10^4 \text{ ms}^{-1} \qquad y = 0.02701 \qquad z = -1.61 \times 10^4 \text{ ms}^{-1} \tag{35}$$

This model provides a reasonable approximation of drag dynamics for orbits of eccentricity between 0.1 and 0.9 and perigee height between 200 and 900 kilometers.

VI.B. The Harris-Priester Atmospheric Density Model

Deriving an STM from the dynamic model described in Eq. 34 requires a model for the atmospheric density at the orbit perigee. According to the Harris-Priester model,[36] the atmospheric density, ρ, is given as

$$\rho = \rho_{min}(h) + (\rho_{max}(h) - \rho_{min}(h))\left(\frac{\mathbf{r}\cdot\hat{\mathbf{r}}_{bulge}}{2||\mathbf{r}||} + \frac{1}{2}\right)^{m/2} \qquad \hat{\mathbf{r}}_{bulge} = \begin{bmatrix} \cos 30^o & -\sin 30^o & 0 \\ \sin 30^o & \cos 30^o & 0 \\ 0 & 0 & 1 \end{bmatrix} \hat{\mathbf{r}}_{sun} \tag{36}$$

where ρ_{min} and ρ_{max} are piecewise log-linear functions that bound the atmospheric density as a function of the geodetic height, h. Additionally, $\mathbf{r}$ denotes the position vector of the spacecraft, $\hat{\mathbf{r}}_{sun}$ denotes the pointing vector to the sun, and $\hat{\mathbf{r}}_{bulge}$ denotes the pointing vector the apex of the diurnal bulge, where the atmospheric density is maximized for a given geodetic height. The rotation serves to place the bulge apex at 2:00 pm local time, which is roughly when the atmosphere is hottest. Finally, the exponent m varies from 2 for equatorial orbits to 6 for polar orbits. From Eq. 36 it is evident that the Harris-Priester model is neither closed-form nor differentiable for two reasons. First, ρ_{min} and ρ_{max} are piecewise functions which have discontinuities in their derivatives. These functions take the form

$$\begin{aligned} \rho_{min}(h) &= \rho_{min}(h_i)\exp\left(\frac{h-h_i}{H_{mi}}\right), \qquad h_i \le h \le h_{i+1} \\ \rho_{max}(h) &= \rho_{max}(h_i)\exp\left(\frac{h-h_i}{H_{Mi}}\right), \qquad h_i \le h \le h_{i+1} \end{aligned} \tag{37}$$

where $\rho_{min}(h_i)$, $\rho_{max}(h_i)$, and h_i are pre-tabulated values. The scale heights H_{mi} and H_{Mi} are computed to ensure that the resulting density profile is continuous. The second problem is that the geodetic height

is generally computed using an iterative algorithm which is not differentiable. While these issues have been addressed in a modified form of the Harris-Priester model by Hatten and Russell,[37] for this paper a simpler model is sought in order to demonstrate the STM derivation method. Accordingly, a simplified, closed-form, differentiable approximation of the Harris-Priester density model is described in the following.

The discontinuities in the derivatives of ρ_{min} and ρ_{max} are corrected by computing global approximations. A convenient feature of the original Harris-Priester model is that the scale height monotonically increases with geodetic height, resulting in a relatively smooth density profile. Accordingly, functions of the form

$$\rho_{min}(h) = \exp(b_1 h^{c_1}); \qquad \rho_{max}(h) = \exp(b_2 h^{c_2}) \tag{38}$$

can approximate the piecewise functions within 6% on average for heights of at least 200 km. The empirical constants b_1, b_2, c_1, and c_2 are computed from a simple regression fit and are given as

$$b_1 = -0.7443 \qquad c_1 = 0.278 \qquad b_2 = -1.345 \qquad c_2 = 0.2286. \tag{39}$$

The second issue is resolved by developing a closed-form, differential approximation of the geodetic height of the perigee. The geodetic height depends only on the orbit radius and latitude of the spacecraft. Specifically, for a fixed radius the geodetic height is at a minimum over the equator and maximum over the poles. It follows that the geodetic height of the perigee can be approximated by a function of the form

$$h_p = a(1-e) - R_E + \Delta h_{obl} \sin^2(i) \sin^2(\omega) \tag{40}$$

where Δh_{obl} denotes the difference between earth's equatorial and polar radii, which is approximately 21385 meters. Finally, in the simplified model the exponent m is assumed to be 2 for all orbits to simplify the necessary partial derivatives. The following substitutions are employed in order to simplify subsequent derivations.

$$C = 1 + \hat{\mathbf{r}}_{bulge} \cdot \begin{pmatrix} \cos(\omega)\cos(\Omega) - \sin(\omega)\cos(i)\sin(\Omega) \\ \cos(\omega)\sin(\Omega) + \sin(\omega)\cos(i)\cos(\Omega) \\ \sin(\omega)\sin(i) \end{pmatrix} \qquad C_i = \frac{\partial C}{\partial i} = \hat{\mathbf{r}}_{bulge} \cdot \begin{pmatrix} \sin(\omega)\sin(i)\sin\Omega) \\ -\sin(\omega)\sin(i)\cos(\Omega) \\ \sin(\omega)\cos(i) \end{pmatrix} \tag{41}$$

$$C_\omega = \frac{\partial C}{\partial \omega} = \hat{\mathbf{r}}_{bulge} \cdot \begin{pmatrix} -\sin(\omega)\cos(\Omega) - \cos(\omega)\cos(i)\sin(\Omega) \\ -\sin(\omega)\sin(\Omega) + \cos(\omega)\cos(i)\cos(\Omega) \\ \cos(\omega)\sin(i) \end{pmatrix} \tag{42}$$

$$C_\Omega = \frac{\partial C}{\partial \Omega} = \hat{r}_{bulge} \cdot \begin{pmatrix} -\cos(\omega)\sin(\Omega) - \sin(\omega)\cos(i)\cos(\Omega) \\ \cos(\omega)\cos(\Omega) - \sin(\omega)\cos(i)\sin(\Omega) \\ 0 \end{pmatrix} \tag{43}$$

$$D = \frac{1}{2}(\rho_{max}(h_p) - \rho_{min}(h_p)) \qquad \rho_p = \rho_{min}(h_p) + CD \qquad f' = \frac{\partial f}{\partial e} = xye^{y-1} \tag{44}$$

$$\rho'_{min} = \frac{\partial \rho_{min}(h_p)}{\partial h_p} = \rho_{min} b_1 c_1 h_p^{c_1 - 1} \qquad \rho'_{max} = \frac{\partial \rho_{max}(h_p)}{\partial h_p} = \rho_{max} b_2 c_2 h_p^{c_2 - 1} \tag{45}$$

$$\rho'_p = \rho'_{min} + \frac{1}{2}(\rho'_{max} - \rho'_{min})C \qquad H_a = \frac{\partial h_p}{\partial a} = 1 - e \qquad H_e = \frac{\partial h_p}{\partial e} = -a \tag{46}$$

$$H_i = \frac{\partial h_p}{\partial i} = 2\Delta h_{obl} \sin^2(\omega)\sin(i)\cos(i) \qquad H_\omega = \frac{\partial h_p}{\partial \omega} = 2\Delta h_{obl} \sin(\omega)\cos(\omega)\sin^2(i) \tag{47}$$

VI.C. Singular State Derivation

Because the STMs derived in this section include a DMS differential drag model, it is necessary to include the differential ballistic properties of the chief and deputy in the state definition. This is accomplished by including the differential ballistic coefficient, δB, defined as

$$\delta B = \frac{B_d - B_c}{B_c} \tag{48}$$

in the relative state. The differential drag plant matrix for the singular state is derived as follows. First, because a and e are the only orbit elements with nonzero time derivatives due to atmospheric drag, the singular state time derivatives are given as

$$\begin{pmatrix} \delta\dot{\boldsymbol{\alpha}}_s \\ \delta\dot{B} \end{pmatrix} = B_d f_d \rho_{pd} \begin{pmatrix} \frac{a_d}{a_c(1-e_c)} \\ 0 \\ 1 \\ \mathbf{0}^{4\times 1} \end{pmatrix} - B_c f_c \rho_{pc} \begin{pmatrix} \frac{a_d}{a_c(1-e_c)} \\ 0 \\ 1 \\ \mathbf{0}^{4\times 1} \end{pmatrix}. \tag{49}$$

The first-order Taylor expansion of Eq. 49 about zero separation is given as

$$\begin{pmatrix} \delta\dot{\boldsymbol{\alpha}}_s \\ \delta\dot{B} \end{pmatrix} = \mathbf{A}_s^{drag}(\boldsymbol{\alpha}_c, \hat{\mathbf{r}}_{bulge}) \begin{pmatrix} \delta\boldsymbol{\alpha}_s \\ \delta B \end{pmatrix} + \mathcal{O}(\delta\alpha_s^2)$$

$$\mathbf{A}_s^{drag}(\boldsymbol{\alpha}_c, \hat{\mathbf{r}}_{bulge}) = B \left[\begin{array}{ccccccc} fa\rho_p' & 0 & \frac{1}{1-e}(f'\rho_p + \frac{f\rho_p}{1-e} - af\rho_p') & \frac{1}{1-e}f(\rho_p' H_\omega + DC_\omega) & \frac{1}{1-e}f(\rho_p' H_i + DC_i) & \frac{1}{1-e}fDC_\Omega & \frac{f\rho_p}{1-e} \\ 0 & 0 & 0 & 0 & 0 & 0 & 0 \\ a(1-e)f\rho_p' & 0 & f'\rho_p - af\rho_p' & f(\rho_p' H_\omega + DC_\omega) & f(\rho_p' H_i + DC_i) & fDC_\Omega & f\rho_p \\ \hline \multicolumn{7}{c}{\mathbf{0}^{4\times 7}} \end{array}\right] \tag{50}$$

Once again the range of applicability can be determined by examining the higher-order terms of the Taylor expansion. First, it is evident from Eq. 49 that the secular drift of the ROE due to differential drag is invariant of the mean anomaly of both spacecraft. Accordingly, all partial derivatives of any order with respect to δM will be zero. Additionally, the second order partial derivatives of the state rates with respect to δB are given as

$$\frac{\partial^2 \delta\dot{a}}{\partial \delta B^2} = \frac{\partial^2 \delta\dot{a}}{\partial B_d^2}\frac{\partial^2 B_d}{\partial \delta B^2} = 0 \qquad \frac{\partial^2 \delta\dot{e}}{\partial \delta B^2} = \frac{\partial^2 \delta\dot{a}}{\partial B_d^2}\frac{\partial^2 B_d}{\partial \delta B^2} = 0, \tag{51}$$

which is expected since the dynamic model defined in Eq. 34 is linear with respect to B. However, second order partial derivatives with respect to combinations of state components including δB (e.g. $\delta a \delta B$) will be nonzero. Thus, this model admits large values of δB as long as the separation in all other terms except δM are small.

It is evident that directly solving for the exponential of the plant matrix for the combined effects of Keplerian relative motion, J_2, and differential drag is difficult. However, the problem can be greatly simplified by considering the properties of the atmospheric density model. Recall that the atmospheric density is an exponential function of geodetic height and varies with the dot product of the position vector and the pointing vector to the apex of the diurnal bulge. Also, a difference in perigee radii of the chief and deputy will manifest in the δa and δe components, while a difference in orbit orientation manifests as differences in $\delta\omega$, δi, and $\delta\Omega$. It follows that the partial derivatives with respect to δa and δe are orders-of-magnitude larger than the partial derivatives with respect to $\delta\omega$, δi, and $\delta\Omega$. These smaller partial derivatives can be neglected with little impact on propagation accuracy. Under this assumption the differential drag plant matrix simplifies to

$$\mathbf{A}_s^{drag}(\boldsymbol{\alpha}_c, \hat{\mathbf{r}}_{bulge}) = B \left[\begin{array}{ccc:c:c} fa\rho_p' & 0 & \frac{1}{1-e}(f'\rho_p + \frac{f\rho_p}{1-e} - af\rho_p') & & \frac{f\rho_p}{1-e} \\ 0 & 0 & 0 & \mathbf{0}^{3\times 3} & 0 \\ a(1-e)f\rho_p' & 0 & f'\rho_p - af\rho_p' & & f\rho_p \\ \hline \multicolumn{5}{c}{\mathbf{0}^{4\times 7}} \end{array}\right]. \tag{52}$$

Unlike in the derivation of the J_2 STMs, these differential equations are time varying due to the circularization of the chief orbit due to atmospheric drag and the motion of the sun. However, for reasonable propagation times the changes in a and e are small relative to their respective magnitudes and the location of the sun varies slowly with time. Thus, in order to produce an analytically tractable solution it is reasonable to assume that the terms of this plant matrix are constant. Additionally, it is assumed that the eccentricity and semi-major axis of the chief orbit are constant so that the J_2-perturbed plant matrices remain time-invariant when drag is included.

Recall from the previous section that δa and δe are unaffected by J_2. It follows that an STM including the effects of J_2 and differential drag can be derived in two steps. First, a drag-only STM, $\boldsymbol{\Phi}_s^{drag}(\boldsymbol{\alpha}_c(t_i), \tau)$,

is derived which provides the time history of δa and δe. Second, the change in the state due to Keplerian motion and J_2 is computed by integrating the product of the appropriate plant matrices and the resulting state history. The drag-only STM can be computed in closed-form from the plant matrix using eigenvalue decomposition. For clarity, the following derivation is expressed in terms of the non-zero partial derivatives in Eq. 52, which are given as

$$\begin{aligned} \frac{\partial \delta \dot{a}}{\partial \delta a} &= Bfa\rho_p' \qquad \frac{\partial \delta \dot{a}}{\partial \delta e} = \frac{B}{1-e}(f'\rho_p + \frac{f\rho_p}{1-e} - af\rho_p') \qquad \frac{\partial \delta \dot{a}}{\partial \delta B} = \frac{Bf\rho_p}{(1-e)} \\ \frac{\partial \delta \dot{e}}{\partial \delta a} &= a(1-e)Bf\rho_p' \qquad \frac{\partial \delta \dot{e}}{\partial \delta e} = B(f'\rho_p - af\rho_p') \qquad \frac{\partial \delta \dot{e}}{\partial \delta B} = Bf\rho_p. \end{aligned} \tag{53}$$

The eigenvalues of the plant matrix are given as

$$\begin{aligned} \lambda_1 &= \frac{1}{2}\left(\frac{\partial \delta \dot{a}}{\partial \delta a} + \frac{\partial \delta \dot{e}}{\partial \delta e} - \sqrt{\frac{\partial \delta \dot{a}}{\partial \delta a}^2 - 2\frac{\partial \delta \dot{a}}{\partial \delta a}\frac{\partial \delta \dot{e}}{\partial \delta e} + 4\frac{\partial \delta \dot{a}}{\partial \delta e}\frac{\partial \delta \dot{e}}{\partial \delta a} + \frac{\partial \delta \dot{e}}{\partial \delta e}^2}\right) \\ \lambda_2 &= \frac{1}{2}\left(\frac{\partial \delta \dot{a}}{\partial \delta a} + \frac{\partial \delta \dot{e}}{\partial \delta e} + \sqrt{\frac{\partial \delta \dot{a}}{\partial \delta a}^2 - 2\frac{\partial \delta \dot{a}}{\partial \delta a}\frac{\partial \delta \dot{e}}{\partial \delta e} + 4\frac{\partial \delta \dot{a}}{\partial \delta e}\frac{\partial \delta \dot{e}}{\partial \delta a} + \frac{\partial \delta \dot{e}}{\partial \delta e}^2}\right) \end{aligned} \tag{54}$$

and the drag-only STM for the singular state, $\boldsymbol{\Phi}_s^{drag}(\boldsymbol{\alpha}_c(t_i), \tau)$, can be written as

$$\boldsymbol{\Phi}_s^{drag}(\boldsymbol{\alpha}_c(t_i), \hat{\mathbf{r}}_{bulge}, \tau) = \left[\begin{array}{ccc:c:c} c_{111}e^{\lambda_1\tau} + c_{112}e^{\lambda_2\tau} & 0 & c_{121}e^{\lambda_1\tau} + c_{122}e^{\lambda_2\tau} & & c_{131}e^{\lambda_1\tau} + c_{132}e^{\lambda_2\tau} + c_{133} \\ 0 & 1 & 0 & \mathbf{0}^{3\times3} & 0 \\ c_{211}e^{\lambda_1\tau} + c_{212}e^{\lambda_2\tau} & 0 & c_{221}e^{\lambda_1\tau} + c_{222}e^{\lambda_2\tau} & & c_{231}e^{\lambda_1\tau} + c_{232}e^{\lambda_2\tau} + c_{233} \\ \hdashline \multicolumn{3}{c:}{\mathbf{0}^{4\times3}} & \multicolumn{2}{c}{\mathbf{I}^{4\times4}} \end{array}\right] \tag{55}$$

where the constants c are functions of the terms of the plant matrix and are given in Appendix B. Next, the changes in δM, $\delta\omega$, and $\delta\Omega$ due to Keplerian motion and J_2 are computed by multiplying the appropriate plant matrices by the integral of the profiles produced by differential drag. This integral is given as

$$\int_0^\tau \boldsymbol{\Phi}_s^{drag}(\boldsymbol{\alpha}_c(t_i), \hat{\mathbf{r}}_{bulge}, t)dt = \left[\begin{array}{ccc:c:c} c_{111}\frac{e^{\lambda_1\tau}-1}{\lambda_1} + c_{112}\frac{e^{\lambda_2\tau}-1}{\lambda_2} & 0 & c_{121}\frac{e^{\lambda_1\tau}-1}{\lambda_1} + c_{122}\frac{e^{\lambda_2\tau}-1}{\lambda_2} & & c_{131}\frac{e^{\lambda_1\tau}-1}{\lambda_1} + c_{132}\frac{e^{\lambda_2\tau}-1}{\lambda_2} + c_{133}\tau \\ 0 & \tau & 0 & \mathbf{0}^{3\times3} & 0 \\ c_{211}\frac{e^{\lambda_1\tau}-1}{\lambda_1} + c_{212}\frac{e^{\lambda_2\tau}-1}{\lambda_2} & 0 & c_{221}\frac{e^{\lambda_1\tau}-1}{\lambda_1} + c_{222}\frac{e^{\lambda_2\tau}-1}{\lambda_2} & & c_{231}\frac{e^{\lambda_1\tau}-1}{\lambda_1} + c_{232}\frac{e^{\lambda_2\tau}-1}{\lambda_2} + c_{233}\tau \\ \hdashline \multicolumn{3}{c:}{\mathbf{0}^{4\times3}} & \multicolumn{2}{c}{\mathbf{I}^{4\times4}\tau} \end{array}\right]. \tag{56}$$

Finally, the complete DMS STM including the effects of Keplerian motion, J_2, and differential drag on the singular state is given as

$$\boldsymbol{\Phi}_s^{J_2+drag}(\boldsymbol{\alpha}_c(t_i), \hat{\mathbf{r}}_{bulge}, \tau) = \boldsymbol{\Phi}_s^{drag}(\boldsymbol{\alpha}_c(t_i), \hat{\mathbf{r}}_{bulge}, \tau) + \bar{\mathbf{A}}_s^{kep+J_2}(\boldsymbol{\alpha}_c(t_i)) \int_0^\tau \boldsymbol{\Phi}_s^{drag}(\boldsymbol{\alpha}_c(t_i), \hat{\mathbf{r}}_{bulge}, t)dt \tag{57}$$

with

$$\bar{\mathbf{A}}_s^{kep+J_2}(\boldsymbol{\alpha}_c(t_i)) = \left[\begin{array}{c:c} \mathbf{A}^{kep}(\boldsymbol{\alpha}_c(t_i)) + \mathbf{A}_s^{J_2}(\boldsymbol{\alpha}_c(t_i)) & \mathbf{0}^{6\times1} \\ \hdashline \mathbf{0}^{1\times6} & 0 \end{array}\right] \tag{58}$$

for dimensional consistency.

VI.D. Quasi-Nonsingular and Nonsingular State Derivations

Recall that δa is included in all state definitions and that δe, $\delta e_x'$, and $\delta e_x'^*$ are all equivalent to first order. It follows that the plant matrix in Eq. 52 is applicable to the modified forms of the quasi-nonsingular and nonsingular states without modification. Thus, the state-specific subscript is hereafter dropped on the drag-only STM. The DMS STMs for the quasi-nonsingular and nonsingular ROE including are assembled in the same manner as their J_2-perturbed counterparts in Eqs. 24 and 30 and are given as

$$\boldsymbol{\Phi}^{J_2+drag}(\boldsymbol{\alpha}_c(t_i), \hat{\mathbf{r}}_{bulge}, \tau) = \bar{\mathbf{J}}^{-1}(\boldsymbol{\alpha}_c(t_i) + \dot{\boldsymbol{\alpha}}_c(t_i)\tau)\boldsymbol{\Phi}'^{J_2+drag}(\boldsymbol{\alpha}_c(t_i), \hat{\mathbf{r}}_{bulge}, \tau)\bar{\mathbf{J}}(\boldsymbol{\alpha}_c(t_i)) \tag{59}$$

with

$$\boldsymbol{\Phi}'^{J_2+drag}(\boldsymbol{\alpha}_c(t_i), \hat{\mathbf{r}}_{bulge}, \tau) = \boldsymbol{\Phi}^{drag}(\boldsymbol{\alpha}_c(t_i), \hat{\mathbf{r}}_{bulge}, \tau) + \bar{\mathbf{A}}^{kep+J_2}(\boldsymbol{\alpha}_c(t_i)) \int_0^\tau \boldsymbol{\Phi}^{drag}(\boldsymbol{\alpha}_c(t_i), \hat{\mathbf{r}}_{bulge}, t)dt \tag{60}$$

and

$$\bar{\mathbf{A}}^{kep+J_2}(\boldsymbol{\alpha}_c(t_i)) = \left[\begin{array}{c:c} \mathbf{A}^{kep}(\boldsymbol{\alpha}_c(t_i)) + \mathbf{A}^{J_2}(\boldsymbol{\alpha}_c(t_i)) & \mathbf{0}^{6\times 1} \\ \hdashline \mathbf{0}^{1\times 6} & 0 \end{array}\right] \quad \bar{\mathbf{J}}(\boldsymbol{\alpha}_c(t)) = \left[\begin{array}{c:c} \mathbf{J}(\boldsymbol{\alpha}_c(t)) & \mathbf{0}^{6\times 1} \\ \hdashline \mathbf{0}^{1\times 6} & 1 \end{array}\right] \tag{61}$$

for dimensional consistency.

VII. Density-Model-Free Differential Drag in Eccentric Orbits

The STMs derived in the previous section assume an a-priori model relating the effects of differential drag to δB. However, it is known that the density of the atmosphere can vary widely due to solar activity and other effects, rendering development of an accurate differential drag model difficult. This problem can be mitigated by using a density-model-free formulation of the effects of differential drag on eccentric orbits to derive DMF-E STMs. This approach requires a ROE state augmented with the time derivative of the relative semi-major axis, denoted $\delta\dot{a}_{drag}$, which can be estimated by the relative navigation system in-flight. Recalling that atmospheric drag circularizes eccentric orbits, the relative dynamics must satisfy

$$\delta\dot{e} = (1-e)\delta\dot{a}_{drag} \tag{62}$$

regardless of the atmospheric density. It follows that the differential drag dynamics are governed by the new DMF-E plant matrix given as

$$\begin{pmatrix} \delta\dot{\boldsymbol{\alpha}} \\ \delta\ddot{a}_{drag} \end{pmatrix} = \mathbf{A}^{drag'}(\boldsymbol{\alpha}_c(t)) \begin{pmatrix} \delta\boldsymbol{\alpha} \\ \delta\dot{a}_{drag} \end{pmatrix} \qquad \mathbf{A}^{drag'}(\boldsymbol{\alpha}_c(t)) = \left[\begin{array}{c:c} \mathbf{0}^{3\times 6} & \begin{matrix} 1 \\ 0 \\ 1-e \end{matrix} \\ \hdashline \mathbf{0}^{4\times 6} & \mathbf{0}^{4\times 1} \end{array}\right]. \tag{63}$$

As before, this plant matrix is valid for the singular state and modified forms of the quasi-nonsingular and nonsingular states without modification because δe, $\delta e'_x$, and $\delta e'^*_x$ are equivalent to first order. Because of the simple structure of the plant matrix, the drag-only DMF-E STM is given as

$$\boldsymbol{\Phi}^{drag'}(\boldsymbol{\alpha}_c(t_i), \tau) = \mathbf{I}^{7\times 7} + \mathbf{A}^{drag'}(\boldsymbol{\alpha}_c(t_i))\tau \tag{64}$$

and its integral is given as

$$\int_0^\tau \boldsymbol{\Phi}^{drag'}(\boldsymbol{\alpha}_c(t_i), t)dt = \mathbf{I}^{7\times 7}\tau + \mathbf{A}^{drag'}(\boldsymbol{\alpha}_c(t_i))\frac{\tau^2}{2}. \tag{65}$$

The complete DMF-E STMs are computed by substituting the matrices in Eqs. 64 and 65 for their appropriate counterparts in Eqs. 57 and 59. The individual terms of these STMs are provided in Appendix C. The key limitations of the these STMs are as follows. First, these models are only valid as long as the semi-major axis and eccentricity of the chief orbit and the time derivative of the relative semi-major axis can be treated as constant. Additionally, these STMs require orbit eccentricities large enough that the circularization assumptions holds. The authors have found from simulations that this is true for $e \geq 0.05$.

VII.A. Relative Motion Description

Once again, it is instructive to consider the geometry of the resulting relative motion including effects of Kepler, J_2, and differential drag. The relative motion produced by the DMF-E STMs is illustrated in Fig. 2 for the singular (left), quasi-nonsingular (center), and nonsingular (right) ROE. As before, the dotted lines denote individual effects and the solid lines denote combined trajectories. First, consider the effects of differential drag on the quasi-nonsingular ROE. Compared to the evolution shown in Fig. 1, there are three new effects caused by differential drag: 1) a linear drift of δa, 2) a quadratic drift in $\delta\lambda$ due to the coupling between differential drag and Keplerian relative motion, and 3) a linear drift of the relative eccentricity vector parallel to the phase angle of the chief argument of perigee. The magnitudes of the drifts of the relative semi-major axis and relative eccentricity vector are related by the circularization constraint described in Eq. 62. The effects of differential drag on the singular and nonsingular states follow the same pattern described in

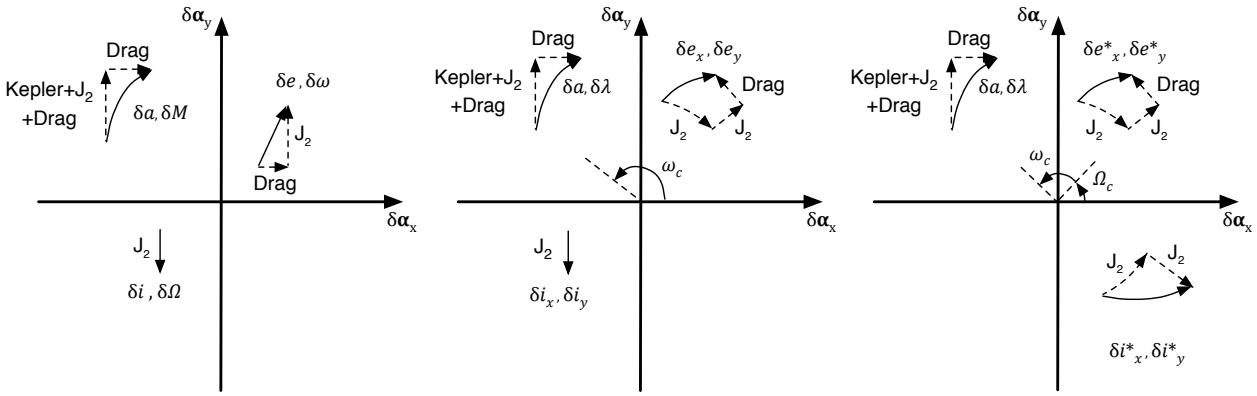

Figure 2. Combined effects of Keplerian relative motion, J_2, and differential drag in eccentric orbits on singular (left), quasi-nonsingular (center), and nonsingular (right) ROE states. Dashed lines denote individual effects and solid lines denote combined trajectories.

Sec. V. There are additional terms in these STMs that are quadratic in time which derive from the coupling between drag and J_2, but because the secular drifts due to drag are already small and the quadratic terms are multiplied by κ, these terms are generally negligible unless the propagation time is very long. Overall, the relative motion produced by these STMs is quite simple and allows useful geometric intuition regarding the combined effects of the J_2 and differential drag perturbations. This intuition suggests that in principle it is possible to select absolute and relative orbits such that the effects of differential drag and J_2 counteract each other, producing frozen relative orbits.

VIII. Generalization to Orbits of Arbitrary Eccentricity

The DMF-E STMs presented in the preceding section are derived under the assumption that the orbit is circularizing, which is only valid for orbits with significant eccentricity. As the eccentricity approaches zero, the effect of atmospheric drag at the orbit apogee becomes non-negligible and the perigee height begins to decrease. Additionally, the presence of the diurnal bulge, where the atmosphere on the illuminated side of earth is denser for a given altitude, causes the argument of perigee to vary. To address these issues, the following analysis derives STMs incorporating a DMF formulation of the effects of differential drag on arbitrarily eccentric orbits. This DMF-A model is inspired by the work done by Gaias on modeling relative motion subject to time-varying differential drag in near circular orbits.[27] Specifically, the state is augmented with three drift terms as opposed to the single term used in the previous section. For example, the singular ROE are augmented with the time derivatives of the relative semi-major axis, $\delta\dot{a}_{drag}$, differential eccentricity, $\delta\dot{e}_{drag}$, and differential argument of perigee, $\delta\dot{\omega}_{drag}$, due to differential drag. The drag dynamics are governed by the new DMF-A plant matrix given as

$$\begin{pmatrix} \delta\dot{\boldsymbol{\alpha}}_s \\ \delta\ddot{a}_{drag} \\ \delta\ddot{e}_{drag} \\ \delta\ddot{\omega}_{drag} \end{pmatrix} = \mathbf{A}_s^{drag*} \begin{pmatrix} \delta\boldsymbol{\alpha}_s \\ \delta\dot{a}_{drag} \\ \delta\dot{e}_{drag} \\ \delta\dot{\omega}_{drag} \end{pmatrix} \qquad \mathbf{A}_s^{drag*} = \left[\begin{array}{c:ccc} & 1 & 0 & 0 \\ & 0 & 0 & -1 \\ \mathbf{0}^{4\times 6} & 0 & 1 & 0 \\ & 0 & 0 & 1 \\ \hdashline \mathbf{0}^{5\times 6} & \multicolumn{3}{c}{\mathbf{0}^{5\times 3}} \end{array}\right]. \tag{66}$$

In this plant matrix the -1 term arises from the behavior of the Gauss variational equations. Specifically, an in-plane impulse will produce equal and opposite changes in the argument of perigee and true anomaly. The mean anomaly and true anomaly can be treated as equal in regard to secular effects. Unlike the derivations provided in previous sections, this plant matrix is not valid for the modified forms of the quasi-nonsingular and nonsingular states, which include the sum of the mean anomaly and argument of perigee in

their definitions. The dynamics of these states are instead given as

$$\begin{pmatrix} \delta\dot{\boldsymbol{\alpha}}_{qns'} \\ \delta\ddot{a}_{drag} \\ \delta\ddot{e}'_{x\,drag} \\ \delta\ddot{e}'_{y\,drag} \end{pmatrix} = \mathbf{A}^{drag*}_{qns'} \begin{pmatrix} \delta\boldsymbol{\alpha}_{qns'} \\ \delta\dot{a}_{drag} \\ \delta\dot{e}'_{x\,drag} \\ \delta\dot{e}'_{y\,drag} \end{pmatrix} \qquad \begin{pmatrix} \delta\dot{\boldsymbol{\alpha}}_{ns'} \\ \delta\ddot{a}_{drag} \\ \delta\ddot{e}'^{*}_{x\,drag} \\ \delta\ddot{e}'^{*}_{y\,drag} \end{pmatrix} = \mathbf{A}^{drag*}_{ns'} \begin{pmatrix} \delta\boldsymbol{\alpha}_{ns'} \\ \delta\dot{a}_{drag} \\ \delta\dot{e}'^{*}_{x\,drag} \\ \delta\dot{e}'^{*}_{y\,drag} \end{pmatrix} \tag{67}$$

with DMF-A plant matrices given as

$$\mathbf{A}^{drag*}_{qns'} = \mathbf{A}^{drag*}_{ns'} = \left[\begin{array}{c:ccc} & 1 & 0 & 0 \\ & 0 & 0 & 0 \\ \mathbf{0}^{4\times 6} & 0 & 1 & 0 \\ & 0 & 0 & 1 \\ \hdashline \mathbf{0}^{5\times 6} & \multicolumn{3}{c}{\mathbf{0}^{5\times 3}} \end{array}\right]. \tag{68}$$

As before, the drag-only DMF-A STM is given as

$$\boldsymbol{\Phi}^{drag*}(\tau) = \mathbf{I}^{9\times 9} + \mathbf{A}^{drag*}\tau. \tag{69}$$

and its integral is given as

$$\int_0^\tau \boldsymbol{\Phi}^{drag*}(t)dt = \mathbf{I}^{9\times 9}\tau + \mathbf{A}^{drag*}\frac{\tau^2}{2}. \tag{70}$$

The complete DMF-A STMs are computed by substituting Eqs. 69 and 70 as appropriate into Eqs. 57 and 59. However, the plant matrices for Keplerian relative motion and J_2 and transformation matrices must be expanded as in Eq. 61 to accommodate the new drag parameters. The individual terms of these DMF-A STMs are provided in Appendix D.

It can be found that neglecting the terms proportional to eccentricity in the quasi-nonsingular STM produces a result very similar to the Gaias[27] STM for near-circular orbits. Specifically, the quasi-nonsingular STM produces the same drift in δa, quadratic drift in $\delta\lambda$, and linear drift of the relative eccentricity vector due to differential drag. The difference between these formulations is that Gaias' model includes an exact linear drift, while the model presented here produces a drift subject to a rotation because it is cast in the modified quasi-nonsingular state. The J_2-dependent terms of these models are identical.

IX. Perturbation Analysis

Because the models presented in this paper include only secular J_2 and differential drag perturbations, it is prudent to identify orbits in which these perturbations dominate the relative motion before proceeding with numerical validation. Specifically, the following analysis aims to identify orbits in which the time-averaged relative accelerations from J_2 and differential drag exceed the magnitude of solar radiation pressure and third-body gravity by at least a factor of 10. In order to perform this analysis it is necessary to make some assumptions about the formation. This analysis assumes a formation consisting of two micro-satellites. The chief satellite has a ballistic coefficient of 0.01 m^2/kg and the differential ballistic coefficient is 0.1. Finally, it is assumed that the inter-spacecraft separation will be on the order of kilometers or less.

First, consider the effect of solar radiation pressure. At a distance of 1 AU from the sun, the solar radiation pressure is given by Vallado[38] as 4.56 μPa. Assuming that the ballistic coefficients for atmospheric drag and solar radiation pressure are equal, the relative acceleration due to solar radiation pressure, δg_{SRP}, is modeled as

$$\delta g_{SRP} = P_{SRP} B_c |\delta B| \tag{71}$$

where P_{SRP} denotes the solar radiation pressure. For the described formation, this yields a relative acceleration of 4e-9 ms^{-2}.

Next, consider third-body gravity perturbation. For spacecraft in earth orbit, lunar gravity is the most significant third-body perturbation. Because of the large distance between the earth and moon, third-body

acceleration is effectively invariant of orbit radius and depends only on the inter-spacecraft separation. The perturbing acceleration from lunar gravity, g_{moon}, is given as

$$g_{moon} = \frac{\mu_{moon}}{r_{moon}^2} \tag{72}$$

where μ_{moon} is the moon's gravitational parameter and r_{moon} is the distance from the spacecraft to the moon. Assuming that the relative position vector is aligned with the pointing vector from the spacecraft to the moon, the relative acceleration due to lunar gravity, δg_{moon}, can be computed by multiplying the derivative of the acceleration by the inter-spacecraft separation, δr, given as

$$\delta g_{moon} = \frac{2\mu_{moon}}{r_{moon}^3}\rho = 1.72 \times 10^{-13} s^{-2} \delta r. \tag{73}$$

It is evident from Eq. 73 that for the described spacecraft the influence of solar radiation pressure will exceed that of third-body gravity from the moon unless the inter-spacecraft separation is on the order of tens of kilometers. Thus, under the aforementioned assumptions the relative motion will be dominated by J_2 and differential drag as long as each of these perturbations produced an average relative acceleration of at least 4e-8 ms^{-2}.

Next, recall the model of the perturbing acceleration due to atmospheric drag described in Eq. 32. Neglecting the variation in density due to differing positions of the spacecraft, the relative acceleration due to differential atmospheric drag, δg_{drag}, can be modeled as

$$\delta g_{drag} = -\frac{1}{2}\rho ||\mathbf{v} - \mathbf{v}_{atm}||^2 |B_c - B_d|. \tag{74}$$

It is immediately evident from Eq. 74 that the average relative acceleration due to differential drag will be a complex function of the orbit semi-major axis and eccentricity. In order to characterize this perturbation, the authors numerically integrated Eq. 74 for a set of orbits with perigee altitudes from 200 to 900 km and eccentricities from 0 to 0.9 using density values from the Harris-Priester model.[36] The time-averaged relative acceleration from these simulations is shown in Fig. 3. The black line indicates the maximum

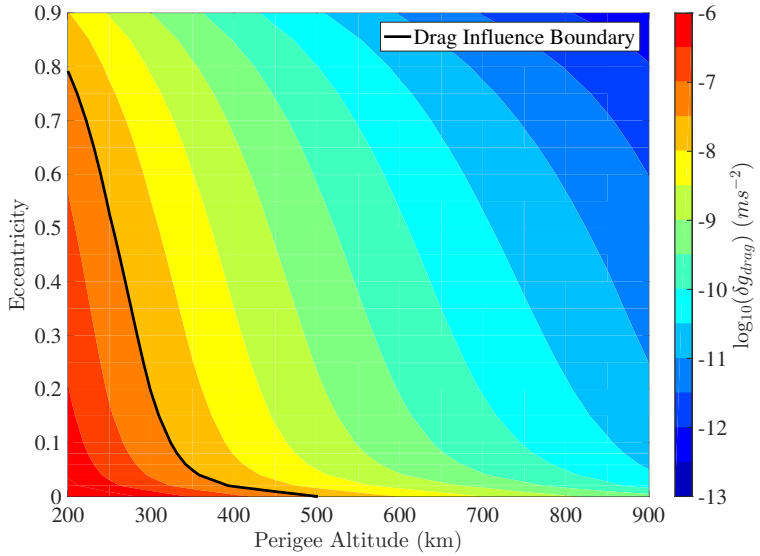

Figure 3. Time-averaged relative acceleration due to differential drag vs perigee altitude and eccentricity for ballistic coefficient of 0.01 m^2/kg and differential ballistic coefficient of 10%.

perigee height for a specified orbit eccentricity that satisfies the requirement that the effect of differential drag is ten times larger than the effect of solar radiation pressure. For near-circular orbits differential drag dominates solar radiation pressure for perigee altitudes as high as 500 km. However, as eccentricity increases to 0.1, the maximum allowable perigee height quickly falls to 300 km. As orbit eccentricity increases to

0.8, the maximum allowable perigee height slowly decreases to 200 km. This behavior is expected because atmospheric drag is only significant near the perigee of eccentric orbits. The decrease in perigee altitude causes an increase in atmospheric density, which compensates for the fact that drag affects a decreasing fraction of the orbit period as eccentricity increases.

Finally, consider the J_2 perturbation. From Vallado,[38] the potential function of the J_2 perturbation, G_{J_2}, is given as

$$G_{J_2} = -\frac{3\mu J_2 R_E^2}{2r^3}\left(\frac{r_z^2}{r^2} - \frac{1}{3}\right) \tag{75}$$

where μ is earth's gravitational parameter, J_2 is the earth oblateness coefficient, R_E is the radius of earth, r is the spacecraft orbit radius, r_z is the z-component of the position vector of the spacecraft in the ECI frame. This potential is maximized if the spacecraft is over one of the poles. In this case, the acceleration due to J_2, g_{J_2}, is given as

$$g_{J_2} = \frac{3\mu J_2 R_E^2}{r^4}. \tag{76}$$

If the relative position vector of the formation is aligned with the radius vector, then the magnitude of the relative acceleration due to J_2, δg_{J_2}, can be computed by multiplying the spacecraft separation by the derivative of the acceleration with respect to the orbit radius, given as

$$\delta g_{J_2} = \frac{12\mu J_2 R_E^2}{r^5}\delta r \tag{77}$$

For an inter-spacecraft separation of 1 km, the effect of J_2 dominates the effect of solar radiation pressure for orbit radii of less than 30,000 km. It follows that spacecraft relative motion is dominated by J_2 and differential drag if the apogee radius of the orbit is no larger than 30,000 km and that the perigee altitude does not exceed the value indicated in Fig. 3 for a specified orbit eccentricity.

X. Validation

At this stage it is necessary to validate the previously described STMs. This is accomplished by comparing the output of an open-loop propagation using each STM with the mean ROE provided by a high-fidelity numerical orbit propagator including a general set of perturbations. Key parameters and perturbation models employed by the numerical propagator are described in Tab. 1. Each of the test cases described

Table 1. Numerical orbit propagator parameters.

Integrator	Runge-Kutta (Dormand-Prince)
Step size	Fixed: 10 sec
Geopotential	GGM05S (20x20)[39]
Atmospheric density	Harris-Priester[36] or Jacchia-Gill[40]
Third body	Lunar and solar point masses, analytical ephemerides
Solar Radiation Pressure	Satellite cross-section normal to the sun, no eclipses

in the following is simulated once with atmospheric density computed from the Harris-Priester model and again with atmospheric density computed from the Jacchia-Gill model in order to assess robustness of the STMs to unmodeled variations in atmospheric density. Simulations are performed for three distinct test cases varying in both separation and eccentricity. The initial chief and relative orbits for these test cases are described in Tab. 2. Each simulation starts on January 1, 2002 at 00:00:00. These test cases are selected to be representative of past and future formation flying missions. Test 1 is representative of a number of science missions conducted in LEO such as TanDEM-X.[2] Test 2 is a notional mission with a moderately eccentric, nearly equatorial orbit and separation of a few kilometers. Finally, Test 3 is modeled after the mDOT[6] mission and features a highly eccentric orbit and large cross-track separation. The chief spacecraft is assumed to have the properties specified in Tab. 3.

Because the STMs include only the secular effects of J_2 and differential drag on the mean ROE, it is necessary to process the results of the numerical orbit propagation to remove periodic effects. The required computation sequence to produce the mean ROE from the numerically propagated trajectory is illustrated in Fig. 4 and is briefly described in the following. First, the initial osculating chief orbit is converted to

Table 2. Initial chief and relative orbits for test cases.

	Chief orbits						Relative orbits						
	a (km)	e	i (^{o})	Ω (^{o})	ω (^{o})	M (^{o})	$a\delta a$ (m)	$a\delta\lambda$ (m)	$a\delta e_x$ (m)	$a\delta e_y$ (m)	$a\delta i_x$ (m)	$a\delta i_y$ (m)	δB
Test 1	6,812	0.005	30	60	180	180	0	0	200	-200	200	-200	0.4
Test 2	8,348	0.2	1	120	120	180	25	4,000	-1,000	1,000	1,000	0	0.2
Test 3	13,256	0.5	45	80	60	180	100	5,000	5,000	5,000	-5,000	20,000	0.1

Table 3. Chief satellite properties.

Mass	Cross-section area	Drag Coefficient	Reflectance Coefficient
100 kg	1 m^2	1	1

an inertial position and velocity, denoted $\mathbf{r}_c$ and $\dot{\mathbf{r}}_c$. Next, the initial chief and relative orbits are used to compute the position and velocity of the deputy, denoted $\mathbf{r}_d$ and $\dot{\mathbf{r}}_d$. The positions and velocities of the chief and deputy are numerically integrated and the resulting trajectories are used to compute the time history of the osculating absolute orbits. The osculating orbit trajectories are then used to compute the osculating ROE trajectories. Because closed-form conversions between mean and osculating states for eccentric orbits perturbed by both J_2 and atmospheric drag are not readily available in literature, the mean ROE are computed by averaging the osculating ROE over a complete orbit. Similarly, the mean chief orbit is computed by averaging all orbit elements except M over one orbit.

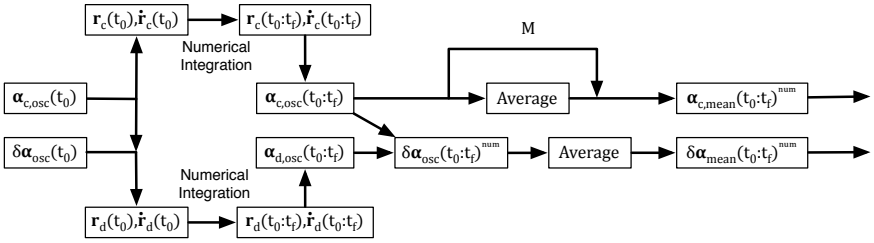

Figure 4. Numerical propagation computation sequence.

In order to accommodate the DMF STMs it is necessary to produce an initial estimate of one or more time derivatives due to differential drag. This is accomplished by dividing the simulation into two phases: 1) an initialization phase beginning at t_0 and ending at t_i, and 2) a propagation phase beginning at t_i and ending at t_f. All simulations include an initialization phase of 4 orbits and a propagation phase of 10 orbits. The estimates of the time derivatives are computed from the known trajectory over the initialization phase. Furthermore, in order to test the robustness of the DMF STMs, the state knowledge over the initialization phase is corrupted by noise consistent with the real-time estimation uncertainty of current state-of-the-art navigation systems. This noise is added after the averaging process in order to produce a conservative estimate of propagation accuracy. Representative noise values are taken from the PRISMA navigation system, which was able to achieve real-time absolute position and velocity estimates with 1-σ uncertainties of 0.5 m and 0.1 cm/s for the chief spacecraft using a sophisticated extended Kalman filter and relative state uncertainties of 5 cm and 0.5 mm/s using differential GNSS techniques.[25] Although achieving such precise estimation in eccentric orbits may not be practical because GNSS signals are less reliable at high altitudes, inclusion of PRISMA-like noise can still provide a useful metric on the sensitivity of these STMs to estimation errors. With this in mind, the necessary computations to produce the noisy data for initial state estimation are illustrated in Fig. 5 and described in the following. First, the mean absolute and relative orbits are converted to position and velocity trajectories for the chief and deputy over the initialization phase. Next, identical absolute state noise values are added to both the chief and deputy states. Afterward, relative state noise is added to only the deputy state. Finally, the chief and relative state estimates are computed from these noisy trajectories. Additionally, an initial estimation error of 1% is included in the differential ballistic coefficient for the DMS STMs. This is comparable to the difference observed in the GRACE satellites, which

were designed to be identical.[41]

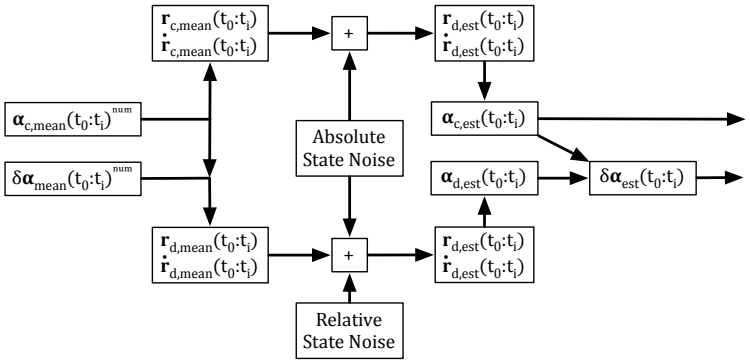

Figure 5. Computation sequence to add representative noise to initialization data.

Next, it is necessary to isolate the effects of differential drag on the ROE over the initialization phase. The state trajectory including only effects of differential drag, $\delta\boldsymbol{\alpha}_{drag}(t)$, is obtained from a function of the noisy initialization data given in state-agnostic form as

$$\delta\boldsymbol{\alpha}_{drag}(t) = \mathbf{J}(\boldsymbol{\alpha}_c(t_i) + \dot{\boldsymbol{\alpha}}_c(t_i)(t-t_i))\delta\boldsymbol{\alpha}_{est}(t) - \mathbf{A}^{J_2}(\boldsymbol{\alpha}_c(t_i))\mathbf{J}(\boldsymbol{\alpha}_c(t_i))\delta\boldsymbol{\alpha}_{est}(t_i)(t-t_i) \qquad t_0 \le t \le t_i. \quad (78)$$

This operation simultaneously casts the quasi-nonsingular and nonsingular states into their modified forms and removes the effects of J_2. If the singular ROE are used, then the transformation matrix $\mathbf{J}$ is the identity matrix. The time derivatives at the start of the open-loop propagation, $\delta\dot{\boldsymbol{\alpha}}_{drag}(t_i)$, are computed by performing a simple linear regression on the appropriate components of $\delta\boldsymbol{\alpha}_{drag}(t)$. The open-loop trajectory for each STM is given as

$$\delta\boldsymbol{\alpha}^{STM}(t) = \boldsymbol{\Phi}(\boldsymbol{\alpha}_c(t_i), t-t_i)\begin{pmatrix}\delta\boldsymbol{\alpha}(t_i)\\ \varnothing \text{ or } \delta B \text{ or } \delta\dot{\boldsymbol{\alpha}}_{drag}(t_i)\end{pmatrix} \qquad t_i \le t \le t_f \quad (79)$$

where the ROE state is augmented with nothing ($\varnothing$) for J_2 STMs, the differential ballistic coefficients for the DMS STMs, or the appropriate time derivatives for the DMF STMs.

Finally, it is necessary to define an appropriate error metric in order to assess STM performance. The error metric is defined as the maximum difference between mean ROE as computed by the numerical propagator and each STM multiplied by the chief mean semi-major axis in order to provide a physical interpretation of the accuracy. This error metric is given as

$$\epsilon_{\delta\alpha_j} = \max_t a^{num}_{c,mean}(t)|\delta\alpha_j^{STM}(t) - \delta\alpha^{num}_{j,mean}(t)| \qquad t_i \le t \le t_f. \quad (80)$$

X.A. Results

Now that the validation scenarios have been defined, the performance of the STMs can be assessed. First, consider the errors produced by the J_2 and DMS STMs given in Tab. 4. The key conclusions that can be drawn from this table are as follows. First, all STMs using the singular state exhibit $\epsilon_{\delta\omega}$ of hundreds of meters for Test 1 and $\epsilon_{\delta\Omega}$ of tens of meters for Test 2 due to their proximity to the circular and equatorial singularities, respectively. The reason that $\epsilon_{\delta\omega}$ is so large for Test 1 is because the argument of perigee becomes extremely sensitive to in-plane perturbations as the orbit eccentricity approaches zero. Thus, differential drag produces large changes in $\delta\omega$ because atmospheric density is non-negligible over the entire orbit. Similarly, the large $\epsilon_{\delta\Omega}$ for Test 2 arises from the sensitivity of the RAAN to perturbing accelerations for near-equatorial orbits. However, the cross-track component of atmospheric drag arises only from the motion of the atmosphere and is much smaller than the in-plane components. This is the reason that $\epsilon_{\delta\Omega}$ for Test 2 are at least an order-of-magnitude smaller than $\epsilon_{\delta\omega}$ for Test 1. It is interesting to note that the STMs for the quasi-nonsingular ROE are well-behaved for Test 2 even though it is singular when the deputy orbit is equatorial. This is because the definition of δi_y scales the difference in RAAN by $\sin(i)$, preventing large errors as Ω becomes more sensitive to perturbations. In light of these observations, the results of STMs using

Table 4. Propagation errors for J_2 and DMS STMs using singular (top), quasi-nonsingular (middle), and nonsingular (bottom) ROE compared to simulations using the Harris-Priester (left) and Jacchia-Gill (right) density models.

		Harris-Priester Atmosphere						Jacchia-Gill Atmosphere					
$\delta\boldsymbol{\alpha}_s$		$\epsilon_{\delta a}$	$\epsilon_{\delta M}$	$\epsilon_{\delta e}$	$\epsilon_{\delta\omega}$	$\epsilon_{\delta i}$	$\epsilon_{\delta\Omega}$	$\epsilon_{\delta a}$	$\epsilon_{\delta M}$	$\epsilon_{\delta e}$	$\epsilon_{\delta\omega}$	$\epsilon_{\delta i}$	$\epsilon_{\delta\Omega}$
STM	Test	(m)	(m)	(m)	(m)	(m)	(m)	(m)	(m)	(m)	(m)	(m)	(m)
J_2	1	38.5	2430.1	13.9	775.6	0.9	5.1	71.0	4718.5	23.4	1293.2	1.0	9.7
	2	37.1	1823.6	30.0	60.8	0.3	63.1	52.2	2455.0	41.9	63.0	0.7	67.4
	3	148.7	7138.9	72.4	10.6	1.5	5.6	211.3	9962.7	103.4	8.8	1.2	7.9
DMS	1	17.9	1455.7	6.7	774.9	0.9	2.3	50.3	3743.2	3.2	1297.6	1.0	6.9
	2	5.9	282.1	4.3	60.4	0.6	58.2	11	512.7	9.0	62.4	0.7	67.1
	3	45.2	1992.2	24.2	4.0	1.5	3.4	17.6	831.7	6.9	3.3	1.2	3.9
$\delta\boldsymbol{\alpha}_{qns}$		$\epsilon_{\delta a}$	$\epsilon_{\delta\lambda}$	$\epsilon_{\delta e_x}$	$\epsilon_{\delta e_y}$	$\epsilon_{\delta i_x}$	$\epsilon_{\delta i_y}$	$\epsilon_{\delta a}$	$\epsilon_{\delta\lambda}$	$\epsilon_{\delta e_x}$	$\epsilon_{\delta e_y}$	$\epsilon_{\delta i_x}$	$\epsilon_{\delta i_y}$
STM	Test	(m)	(m)	(m)	(m)	(m)	(m)	(m)	(m)	(m)	(m)	(m)	(m)
J_2	1	38.5	1808.8	13.5	11.3	0.9	2.5	71.0	3417.0	22.1	17.1	1.0	4.9
	2	37.1	1828.0	25.6	18.7	0.3	1.2	52.2	2455.3	25.6	34.3	0.7	1.2
	3	148.7	7146.1	64.8	34.1	1.5	4.6	211.3	9966.5	90.4	51.6	1.2	6.3
DMS	1	17.9	832.4	6.8	7.7	0.9	1.2	50.3	2439.7	2.2	13.5	1.0	3.5
	2	5.9	278.9	10.3	5.7	0.6	1.1	11.0	509.3	8.9	9.2	0.7	1.2
	3	45.2	1986.8	18.4	15.3	1.5	2.7	17.6	833.6	7.3	3.7	1.2	3.0
$\delta\boldsymbol{\alpha}_{ns}$		$\epsilon_{\delta a}$	$\epsilon_{\delta l}$	$\epsilon_{\delta e_x^*}$	$\epsilon_{\delta e_y^*}$	$\epsilon_{\delta i_x^*}$	$\epsilon_{\delta i_y^*}$	$\epsilon_{\delta a}$	$\epsilon_{\delta l}$	$\epsilon_{\delta e_x^*}$	$\epsilon_{\delta e_y^*}$	$\epsilon_{\delta i_x^*}$	$\epsilon_{\delta i_y^*}$
STM	Test	(m)	(m)	(m)	(m)	(m)	(m)	(m)	(m)	(m)	(m)	(m)	(m)
J_2	1	38.5	1808.2	1.1	17.5	0.9	1.3	71.0	3415.7	0.7	27.9	1.9	2.0
	2	37.1	1828.0	14.0	26.8	0.3	0.3	52.2	2455.3	18.2	38.0	0.6	0.7
	3	148.7	7141.6	25.1	69.5	3.1	1.0	211.3	9961.4	38.1	97.8	4	0.8
DMS	1	17.9	832.1	10.2	1.1	0.3	0.8	50.3	2438.8	9.7	9.4	1.3	1.5
	2	5.9	278.9	0.7	4.3	0.5	0.6	11.0	509.3	3.8	8.4	0.5	0.7
	3	44.8	1973.8	8.0	21.1	1.7	1.1	17.9	846	5.8	7.3	1.9	0.9

singular ROE for Test 1 and Test 2 are neglected in the following discussions of general trends. In general the J_2 STMs produce errors of several kilometers in along-track separation, tens to hundreds of meters in the relative semi-major axis, tens of meters in relative eccentricity, and a few meters in relative inclination. The manifestation of the majority of these errors in the in-plane ROE suggests that these errors are caused primarily by differential drag, as expected from the previous perturbation analysis. The DMS STMs are able to reduce in-plane errors by at least a factor of two for all eccentric orbit cases. The remaining error can be attributed to a combination of the error in the estimate of δB, error in the approximation of atmospheric density at perigee, and errors in the approximation of the dynamics. It is also interesting that these STMs provide a modest improvement for Test 1 even though the governing model is not intended for near-circular orbits.

Next, consider the errors produced by DMF STMs given in Tab. 5. The key conclusions that can be drawn from these results are as follows. First, it is again evident that STMs using singular ROE in near-circular or near-equatorial orbits exhibit large $\epsilon_{\delta\omega}$ and $\epsilon_{\delta\Omega}$, respectively. Accordingly, these results are neglected in the following discussion of general trends for clarity. Next, all DMF STMs provide dramatic reductions of the propagation errors in the relative semi-major axis and along-track separation. Specifically, the worst-case errors in relative semi-major axis and along-track separation are only 5% of their counterparts from the J_2 STMs. The errors in relative eccentricity components are reduced to a few meters in all cases except when the DMF-E STMs are used for Test 1. This is because the DMF-E STMs are derived under the assumption that both orbits are circularizing, which does not hold for near-circular orbits. Additionally, the DMF-A STMs are able to bound the errors in along-track separation to hundreds of meters and all other state components to a few meters in all tested cases. This is comparable to the accuracy of Gaias'

Table 5. Propagation errors for DMF STMs using singular (top), quasi-nonsingular (middle), and nonsingular (bottom) ROE compared to simulations using the Harris-Priester (left) and Jacchia-Gill (right) density models.

		Harris-Priester Atmosphere						Jacchia-Gill Atmosphere					
$\delta\boldsymbol{\alpha}_s$		$\epsilon_{\delta a}$	$\epsilon_{\delta M}$	$\epsilon_{\delta e}$	$\epsilon_{\delta\omega}$	$\epsilon_{\delta i}$	$\epsilon_{\delta\Omega}$	$\epsilon_{\delta a}$	$\epsilon_{\delta M}$	$\epsilon_{\delta e}$	$\epsilon_{\delta\omega}$	$\epsilon_{\delta i}$	$\epsilon_{\delta\Omega}$
STM	Test	(m)	(m)	(m)	(m)	(m)	(m)	(m)	(m)	(m)	(m)	(m)	(m)
DMF-E	1	0.4	769.7	24.8	774.3	0.9	0.3	1.9	1391.3	46.8	1308.3	1.0	0.4
	2	0.6	20.8	0.9	60.5	0.6	58.3	1.3	62.9	1.0	62.3	0.7	67.0
	3	2.9	196.7	2.1	5.6	1.5	3.3	9.5	346.5	7	2.7	1.6	4.4
DMF-A	1	0.4	769.7	2.8	793.2	0.9	0.3	1.9	1391.3	1.7	757.2	1.0	0.4
	2	0.6	20.8	0.2	51.9	0.6	58.3	1.3	62.9	1.4	53.3	0.7	67.0
	3	2.9	196.6	2.1	5.0	1.5	3.3	9.5	346.5	3.7	2.8	1.6	4.4
$\delta\boldsymbol{\alpha}_{qns}$		$\epsilon_{\delta a}$	$\epsilon_{\delta\lambda}$	$\epsilon_{\delta e_x}$	$\epsilon_{\delta e_y}$	$\epsilon_{\delta i_x}$	$\epsilon_{\delta i_y}$	$\epsilon_{\delta a}$	$\epsilon_{\delta\lambda}$	$\epsilon_{\delta e_x}$	$\epsilon_{\delta e_y}$	$\epsilon_{\delta i_x}$	$\epsilon_{\delta i_y}$
STM	Test	(m)	(m)	(m)	(m)	(m)	(m)	(m)	(m)	(m)	(m)	(m)	(m)
DMF-E	1	0.4	25.9	24.6	4.6	0.9	0.2	1.9	83.0	47.0	5.0	1.0	0.2
	2	0.6	24.6	9.5	6.9	0.6	1.1	1.3	67.5	10.2	6.5	0.7	1.2
	3	2.9	202.2	2.1	3.6	1.5	2.6	9.5	343.5	4.5	5.4	1.6	3.3
DMF-A	1	0.4	26	0.4	0.4	0.9	0.2	1.9	82.9	1.7	1.0	1.0	0.2
	2	0.6	24.6	8.3	5.7	0.6	1.1	1.3	67.4	8.9	5.2	0.7	1.2
	3	2.9	202.2	2.9	0.9	1.5	2.6	9.5	346.6	2.2	5.7	2.0	1.2
$\delta\boldsymbol{\alpha}_{ns}$		$\epsilon_{\delta a}$	$\epsilon_{\delta l}$	$\epsilon_{\delta e_x^*}$	$\epsilon_{\delta e_y^*}$	$\epsilon_{\delta i_x^*}$	$\epsilon_{\delta i_y^*}$	$\epsilon_{\delta a}$	$\epsilon_{\delta l}$	$\epsilon_{\delta e_x^*}$	$\epsilon_{\delta e_y^*}$	$\epsilon_{\delta i_x^*}$	$\epsilon_{\delta i_y^*}$
STM	Test	(m)	(m)	(m)	(m)	(m)	(m)	(m)	(m)	(m)	(m)	(m)	(m)
DMF-E	1	0.4	25.9	18.2	17.2	0.4	0.4	1.9	82.9	31.7	35.1	0.3	0.5
	2	0.6	24.6	1.8	0.4	0.5	0.6	1.3	67.5	1.6	0.6	0.5	0.6
	3	2.9	199.1	2.2	2.8	1.6	1.1	11.1	519.8	1.8	6.8	1.9	0.9
DMF-A	1	0.4	25.9	0.5	0.2	0.4	0.4	1.9	82.9	0.9	1.9	0.3	0.5
	2	0.6	24.6	1.0	0.2	0.5	0.6	1.3	67.4	1.4	0.9	0.5	0.6
	3	2.9	199.1	2.1	2.7	1.6	1.1	9.5	346.6	2.9	3.3	2.0	1.2

STM[27] for near-circular orbits, but is valid for any orbit in which J_2 and differential drag are the dominant perturbations. Finally, for mission applications in eccentric orbits, the DMF-E STMs are very nearly as accurate as the DMF-A STMs and can be used to simplify the state estimation problem.

To assess the validity of the assumption in the DMF STMs that the time derivatives of the ROE due to differential drag are constant, consider the evolution of the in-plane quasi-nonsingular ROE for Test 3 in the simulation using the Jacchia-Gill atmosphere plotted in Fig. 6. This plot includes the simulated

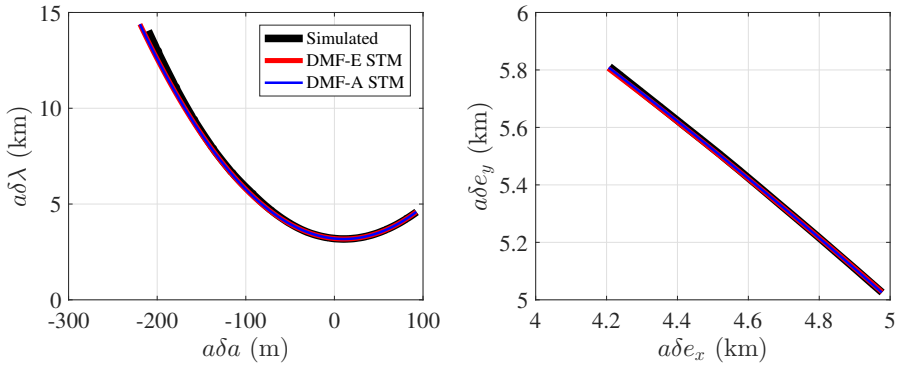

Figure 6. Evolution of the in-plane quasi-nonsingular ROE for Test 3 for a simulation using the Jacchia-Gill atmosphere.

mean ROE (black), ROE computed from the DMF-E STM (red), and ROE computed from the DMF-A STM (blue). It is immediately evident that δa and $\delta\lambda$ follow the parabolic trajectory described in Sec. VII. Similarly, the relative eccentricity vector exhibits a characteristic rotation due to the precession of the argument of perigee. The in-plane propagation errors of the DMF STMs for this scenario are plotted in Fig. 7. The only difference between the performance of the DMF-E and DMF-A STMs is that the DMF-A STM

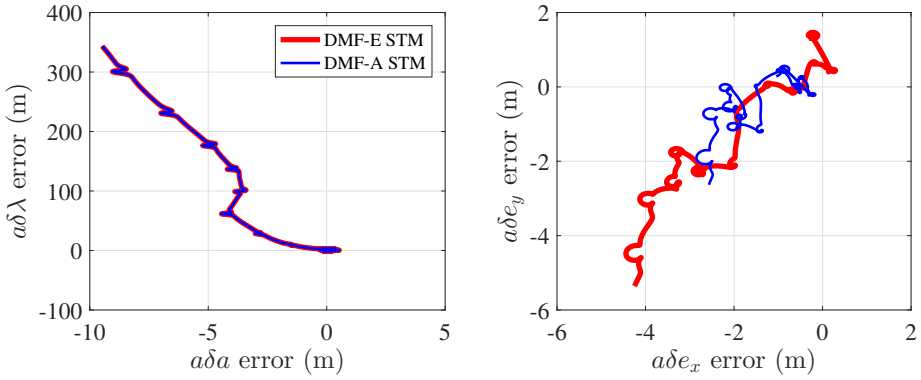

Figure 7. Evolution of the in-plane propagation errors for DMF STMs using quasi-nonsingular ROE for Test 3 for a simulation using the Jacchia-Gill atmosphere.

is able to capture a portion of the drift of the relative eccentricity vector that deviates from the behavior specified by the circularization assumption. It is noteworthy that the error in the relative semi-major axis is not monotonic, and indeed has a brief period where it decreases over the simulation. This behavior occurs because the atmospheric density is changing over the course of the simulation while the STM treats it as constant. These variations in atmospheric density would also explain the seemingly random trajectory of the relative eccentricity error for the DMF-A STM. These behaviors suggest that the propagation error for the DMF-A STM is driven primarily by the time-varying atmospheric density. Improving on these models would therefore require very accurate knowledge of the future behavior of the atmosphere.

In total, several key conclusions about ROE evolution are evident from these results. First, STMs using singular ROE are characterized by poor performance near both of the circular and equatorial singularities. Second, no significant performance difference between STMs using the quasi-nonsingular and nonsingular ROE is observed in all tested scenarios. Third, while all STMs including differential drag are able to reduce propagation error when compared to J_2 STMs, it is found that the DMF STMs clearly outperform the DMS STMs in all tested cases. This suggests that development of a DMS STM that is capable of matching the performance of the DMF STMs would require a complex and computationally expensive atmosphere model. Finally, because these tests include effects of estimation errors consistent with the real-time performance of current state-of-the-art navigation systems, the DMF STMs should be able to produce similar propagation accuracy on orbit.

However, these results are also subject to several limitations which must be addressed. First, the simulated atmosphere models do not include any sudden local variations in atmospheric density (e.g. due to a sudden change in solar activity), and such an event would significantly increase propagation error in all STMs including differential drag. Second, the DMF STMs require an initialization period of several orbits to accurately estimate the required time derivatives due to differential drag. If the initialization period is not sufficiently long, then the drag estimates may be affected by short-period phenomena, reducing propagation accuracy. Third, the performance of the DMF STMs is predicated on the assumption that complete, accurate state estimates are available at regular intervals in order to compute these time derivatives. Some missions may not be able to effectively compute these estimates if the relative state updates are sparse or very noisy. In such cases, a DMS STM with a-priori knowledge of the differential ballistic coefficient may be the best dynamic model. However, the key risk associated with a DMS differential drag model is that if the model overestimates the true density my more than 100%, then the resulting STM will produce errors larger than if drag were ignored altogether.

XI. Conclusion

Future formation-flying missions will require dynamic models that are more accurate, computationally efficient, and have wider ranges of applicability than those available in literature. With this in mind, this paper presents new state transition matrices which model the relative motion of two spacecraft in arbitrarily eccentric orbits perturbed by both J_2 and differential atmospheric drag for three state definitions based on relative orbital elements. These state transition matrices are derived by first linearizing the equations of relative motion and then computing an exact, closed-form solution of the resulting linear differential equations. This paper includes state transition matrices derived using two types differential drag models: 1) a density-model-specific formulation which requires a-priori knowledge of the atmosphere, and 2) density-model-free formulations which require in-flight estimation of time derivatives of specified state components. These models are used to generalize the geometric interpretation of the effects of J_2 and differential drag on relative motion in near-circular orbits provided in previous works to orbits of arbitrary eccentricity. Additionally, this paper harmonizes current literature by demonstrating that several of the state transition matrices published by other authors under different assumptions can be found by subjecting the models presented in this paper to more restrictive assumptions.

The performance of the state transition matrices is validated through comparison with a high-fidelity numerical orbit propagator including a general set of perturbations. In order to demonstrate the robustness of these models, the initial state estimates are corrupted by errors consistent with real-time estimation uncertainties of current state-of-the-art navigation systems. It is found that state transition matrices including density-model-free differential drag are much more accurate than their density-model-specific counterparts and are able to reduce propagation errors in the relative semi-major axis and along-track separation by more than an order of magnitude as compared to models including only J_2. Indeed, the state transition matrices including J_2 and density-model-free differential drag for orbits of arbitrary eccentricity match or exceed the propagation accuracy of state transition matrices available in literature in a wide range of orbit scenarios. Finally, considerations on the evolution of the propagation error for this model suggest that the remaining errors derive primarily from the time variance of the atmospheric density.

The key limitation of the presented models is that their validity is limited to orbits in which the J_2 and atmospheric drag perturbations are dominant. Outside of this region, it becomes necessary to model other perturbations such as solar radiation pressure or third-body gravity from the sun and moon. Future works will incorporate these perturbations into state transition matrices in order to meet the needs of formation-flying mission concepts in highly eccentric orbits such as PROBA-3 and mDOT. The resulting models will allow accurate, computationally efficient modeling of relative motion in a wide variety of orbit scenarios, enabling precise relative navigation on small spacecraft at low cost.

Acknowledgments

This work was supported by a NASA Office of the Chief Technologist's Space Technology Research Fellowship (NSTRF), NASA Grant #NNX15AP70H.

References

[1]Tapley, B. D., Bettadpur, S., Watkins, M., and Reigber, C., "The gravity recovery and climate experiment: Mission overview and early results," *Geophysical Research Letters*, Vol. 31, No. 9, 2004.

[2]Krieger, G., Moreira, A., Fiedler, H., Hajnsek, I., Werner, M., Younis, M., and Zink, M., "TanDEM-X: A satellite formation for high-resolution SAR interferometry," *IEEE Transactions on Geoscience and Remote Sensing*, Vol. 45, No. 11, 2007, pp. 3317–3341.

[3]D'Amico, S., Ardaens, J.-S., and Larsson, R., "Spaceborne autonomous formation-flying experiment on the PRISMA mission," *Journal of Guidance, Control, and Dynamics*, Vol. 35, No. 3, 2012, pp. 834–850.

[4]Burch, J. L., Moore, T. E., Torbert, R. B., and Giles, B. L., "Magnetospheric Multiscale Overview and Science Objectives," *Space Science Reviews*, Vol. 199, No. 1-4, 2016, pp. 5–21.

[5]Llorente, J. S., Agenjo, A., Carrascosa, C., De Negueruela, C., Mestreau-Garreau, A., Cropp, A., and Santovincenzo, A., "PROBA-3: Precise formation flying demonstration mission," *Acta Astronautica*, Vol. 82, No. 1, 2013, pp. 38–46.

[6]Koenig, A. W., D'Amico, S., Macintosh, B., and Titus, C. J., "Formation Design Analysis for a Miniaturized Distributed Occulter/Telescope in Earth Orbit," *International Symposium on Space Flight Dynamics (ISSFD)*, 2015.

[7]D'Amico, S., Pavone, M., Saraf, S., Alhussien, A., Al-Saud, T., Buchman, S., Byer, R., and Farhat, C., "Miniaturized Autonomous Distributed Space System for Future Science and Exploration," *Int. Workshop on Satellite Constellations and Formation Flying, Delft, Netherlands*, 2015.

[8]Sullivan, J., Grimberg, S., and D'Amico, S., "A Survey of Spacecraft Relative Motion Dynamics Models," *Journal of Guidance, Control, and Dynamics*, 2016, Submitted.

[9]Clohessy, W. H. and Wiltshire, R. S., "Terminal Guidance System for Satellite Rendezvous," *Journal of the Aerospace Sciences*, Vol. 29, 1960, pp. 653–658.

[10]Chamberlin, J. A. and Rose, J. T., "Gemini rendezvous program," *Journal of Spacecraft and Rockets*, Vol. 1, No. 1, 1964, pp. 13–18.

[11]Aldrin, B., *Line-of-sight guidance techniques for manned orbital rendezvous*, Ph.D. thesis, Massachusetts Institute of Technology, 1963.

[12]Goodman, J. L., "History of space shuttle rendezvous and proximity operations," *Journal of Spacecraft and Rockets*, Vol. 43, No. 5, 2006, pp. 944–959.

[13]De Bruijn, F., Gill, E., and How, J., "Comparative Analysis of Cartesian and Curvilinear Clohessy-Wiltshire equations," *Journal of Aerospace Engineering, Sciences and Applications*, Vol. 3, No. 2, 2011, pp. 1–15.

[14]Lovell, T. and Tragesser, S., "Guidance for relative motion of low earth orbit spacecraft based on relative orbit elements," *American Institute of Aeronautics and Astronautics*, 2004.

[15]Schweighart, S. A. and Sedwick, R. J., "High-Fidelity Linearized J_2 Model for Satellite Formation Flight," *Journal of Guidance, Control, and Dynamics*, Vol. 25, No. 6, 2002, pp. 1073–1080.

[16]Izzo, D. R., "Formation Flying Linear Modelling," *Dynamics and Control Systems and Structures in Space, King's College, Cambridge*, 2002.

[17]Yamanaka, K. and Ankersen, F., "New State Transition Matrix for Relative Motion on an Arbitrary Elliptical Orbit," *Journal of guidance, control, and dynamics*, Vol. 25, No. 1, 2002, pp. 60–66.

[18]Ardaens, J.-S., D'Amico, S., and Cropp, A., "GPS-based relative navigation for the Proba-3 formation flying mission," *Acta Astronautica*, Vol. 91, 2013, pp. 341–355.

[19]Breger, L. and How, J. P., "Gauss's Variational Equation-Based Dynamics and Control for Formation Flying Spacecraft," *Journal of guidance, control, and dynamics*, Vol. 30, No. 2, 2007, pp. 437–448.

[20]Gim, D.-W. and Alfriend, K. T., "State transition matrix of relative motion for the perturbed noncircular reference orbit," *Journal of Guidance, Control, and Dynamics*, Vol. 26, No. 6, 2003, pp. 956–971.

[21]Gim, D. and Alfriend, K., "Criteria for Best Configuration and Sub-optimal Reconfiguration for MMS Mission," *AAS Spaceflight Mechanics Meeting, Maui, HI*, 2004.

[22]Roscoe, C. W., Westphal, J. J., Griesbach, J. D., and Schaub, H., "Formation Establishment and Reconfiguration Using Differential Elements in J 2-Perturbed Orbits," *Journal of Guidance, Control, and Dynamics*, Vol. 38, No. 9, 2015, pp. 1725–1740.

[23]Gim, D.-W. and Alfriend, K. T., "Satellite relative motion using differential equinoctial elements," *Celestial Mechanics and Dynamical Astronomy*, Vol. 92, No. 4, 2005, pp. 295–336.

[24]Mahajan, B., Vadali, S. R., and Alfriend, K. T., "Analytic Solution for the Satellite Relative Motion: The Complete Zonal Gravitational Problem," *Proceedings of the 26th AAS/AIAA Space Flight Mechanics Meeting, Napa, CA, 2016*, 2016.

[25]D'Amico, S., *Autonomous formation flying in low earth orbit*, TU Delft, Delft University of Technology, 2010.

[26]Gaias, G., D'Amico, S., and Ardaens, J.-S., "Generalised multi-impulsive manoeuvres for optimum spacecraft rendezvous in near-circular orbit," *International Journal of Space Science and Engineering*, Vol. 3, No. 1, 2015, pp. 68–88.

[27]Gaias, G., Ardaens, J.-S., and Montenbruck, O., "Model of J_2 perturbed satellite relative motion with time-varying differential drag," *Celestial Mechanics and Dynamical Astronomy*, Vol. 123, No. 4, 2015, pp. 411–433.

[28]Montenbruck, O., Kirschner, M., D'Amico, S., and Bettadpur, S., "E/I-vector separation for safe switching of the GRACE formation," *Aerospace Science and Technology*, Vol. 10, No. 7, 2006, pp. 628–635.

[29]Montenbruck, O., Kahle, R., D'Amico, S., and Ardaens, J.-S., "Navigation and control of the TanDEM-X formation," *The Journal of the Astronautical Sciences*, Vol. 56, No. 3, 2008, pp. 341–357.

[30]Gaias, G., Ardaens, J.-S., and DAmico, S., "The autonomous vision approach navigation and target identification (AVANTI) experiment: objectives and design," *9th International ESA Conference on Guidance, Navigation & Control Systems, Porto, Portugal*, 2014.

[31]Schaub, H. and Junkins, J. L., *Analytical mechanics of space systems*, AIAA, 2003.

[32]D'Amico, S., "Relative Orbital Elements as Integration Constants of Hills Equations," *DLR, TN*, 2005, pp. 05–08.

[33]D'Amico, S. and Montenbruck, O., "Proximity operations of formation-flying spacecraft using an eccentricity/inclination vector separation," *Journal of Guidance, Control, and Dynamics*, Vol. 29, No. 3, 2006, pp. 554–563.

[34]Brouwer, D., "Solution of the problem of artificial satellite theory without drag," *The Astronomical Journal*, Vol. 64, 1959, pp. 378.

[35]King-Hele, D. G., *Satellite Orbits in an Atmosphere: Theory and application*, Springer Science & Business Media, 1987.

[36]Montenbruck, O. and Gill, E., *Satellite orbits: models, methods and applications*, Springer Science & Business Media, 2012.

[37]Hatten, N. and Russell, R. P., "A Smooth and Robust Harris-Priester Atmospheric Density Model," *Proceedings of the 26th AAS/AIAA Space Flight Mechanics Meeting, Napa, CA, 2016*, 2016.

[38]Vallado, D. A. and McClain, W. D., *Fundamentals of astrodynamics and applications*, Vol. 12, Springer Science & Business Media, 2001.

[39]Tapley, B. D., Flechtner, F., Bettadpur, S. V., and Watkins, M. M., "The status and future prospect for GRACE after the first decade," *AGU Fall Meeting Abstracts*, Vol. 1, 2013, p. 01.

[40]Jacchia, L. G., "Revised static models of the thermosphere and exosphere with empirical profiles," *Res. Space Sci. Spec. Rep. 332*, Smithson. Astrophys. Observ Cambridge, Mass, 1971.

[41]Kirschner, M., Montenbruck, O., and Bettadpur, S., "Flight dynamics aspects of the GRACE formation flying," *2nd International Workshop on Satellite Constellations and Formation Flying*, 2001, pp. 19–20.

A. J_2-Perturbed State Transition Matrices

Simplifying Substitutions

$$\eta = \sqrt{1-e^2} \qquad \kappa = \frac{3}{4}\frac{J_2 R_E^2 \sqrt{\mu}}{a^{7/2}\eta^4} \qquad E = 1+\eta \qquad F = 4+3\eta \qquad G = \frac{1}{\eta^2} \tag{81}$$

$$P = 3\cos^2(i) - 1 \qquad Q = 5\cos^2(i) - 1 \qquad R = \cos(i) \qquad S = \sin(2i) \qquad T = \sin^2(i) \tag{82}$$

$$U = \sin(i) \qquad V = \tan(i/2) \qquad W = \cos^2(i/2) \tag{83}$$

$$\dot{\omega} = \kappa Q \qquad \dot{\Omega} = -2\kappa R \qquad \omega_f = \omega_i + \dot{\omega}\tau \qquad \Omega_f = \Omega_i + \dot{\Omega}\tau \tag{84}$$

$$e_{xi} = e\cos(\omega_i) \qquad e_{yi} = e\sin(\omega_i) \qquad e_{xf} = e\cos(\omega_f) \qquad e_{yf} = e\sin(\omega_f) \tag{85}$$

$$e^*_{xi} = e\cos(\omega_i + \Omega_i) \qquad e^*_{yi} = e\sin(\omega_i + \Omega_i) \qquad e^*_{xf} = e\cos(\omega_f + \Omega_f) \qquad e^*_{yf} = e\sin(\omega_f + \Omega_f) \tag{86}$$

$$i^*_{xi} = \tan(i/2)\cos(\Omega_i) \quad i^*_{yi} = \tan(i/2)\sin(\Omega_i) \quad i^*_{xf} = \tan(i/2)\cos(\Omega_f) \quad i^*_{yf} = \tan(i/2)\sin(\Omega_f) \tag{87}$$

Singular State STM

$$\boldsymbol{\Phi}_s^{J_2}(\boldsymbol{\alpha}_c(t_i),\tau) = \begin{bmatrix} 1 & 0 & 0 & 0 & 0 & 0 \\ -(\frac{3}{2}n + \frac{7}{2}\kappa\eta P)\tau & 1 & 3\kappa e\eta G P\tau & 0 & -3\kappa\eta S\tau & 0 \\ 0 & 0 & 1 & 0 & 0 & 0 \\ -\frac{7}{2}\kappa Q\tau & 0 & 4\kappa e G Q\tau & 1 & -5\kappa S\tau & 0 \\ 0 & 0 & 0 & 0 & 1 & 0 \\ 7\kappa R\tau & 0 & -8\kappa e G R\tau & 0 & 2\kappa U\tau & 1 \end{bmatrix} \tag{88}$$

Quasi-Nonsingular State STM

$$\boldsymbol{\Phi}_{qns}^{J_2}(\boldsymbol{\alpha}_c(t_i),\tau) = \begin{bmatrix} 1 & 0 & 0 & 0 & 0 & 0 \\ -(\frac{3}{2}n + \frac{7}{2}\kappa E P)\tau & 1 & \kappa e_{xi} F G P\tau & \kappa e_{yi} F G P\tau & -\kappa F S\tau & 0 \\ \frac{7}{2}\kappa e_{yf} Q\tau & 0 & \cos(\dot{\omega}\tau) - 4\kappa e_{xi} e_{yf} G Q\tau & -\sin(\dot{\omega}\tau) - 4\kappa e_{yi} e_{yf} G Q\tau & 5\kappa e_{yf} S\tau & 0 \\ -\frac{7}{2}\kappa e_{xf} Q\tau & 0 & \sin(\dot{\omega}\tau) + 4\kappa e_{xi} e_{xf} G Q\tau & \cos(\dot{\omega}\tau) + 4\kappa e_{yi} e_{xf} G Q\tau & -5\kappa e_{xf} S\tau & 0 \\ 0 & 0 & 0 & 0 & 1 & 0 \\ \frac{7}{2}\kappa S\tau & 0 & -4\kappa e_{xi} G S\tau & -4\kappa e_{yi} G S\tau & 2\kappa T\tau & 1 \end{bmatrix} \tag{89}$$

Nonsingular State STM

$$\boldsymbol{\Phi}_{ns}^{J_2}(\boldsymbol{\alpha}_c(t_i),\tau) = \begin{bmatrix} 1 & 0 & 0 & 0 & 0 & 0 \\ \Phi_{21}^{J_2} & 1 & \Phi_{23}^{J_2} & \Phi_{24}^{J_2} & \Phi_{25}^{J_2} & \Phi_{26}^{J_2} \\ \Phi_{31}^{J_2} & 0 & \Phi_{33}^{J_2} & \Phi_{34}^{J_2} & \Phi_{35}^{J_2} & \Phi_{36}^{J_2} \\ \Phi_{41}^{J_2} & 0 & \Phi_{43}^{J_2} & \Phi_{44}^{J_2} & \Phi_{45}^{J_2} & \Phi_{46}^{J_2} \\ \Phi_{51}^{J_2} & 0 & \Phi_{53}^{J_2} & \Phi_{54}^{J_2} & \Phi_{55}^{J_2} & \Phi_{56}^{J_2} \\ \Phi_{61}^{J_2} & 0 & \Phi_{63}^{J_2} & \Phi_{64}^{J_2} & \Phi_{65}^{J_2} & \Phi_{66}^{J_2} \end{bmatrix} \tag{90}$$

$$\Phi_{21}^{J_2} = -\Big(\frac{3}{2}n + \frac{7}{2}\kappa(\eta P + Q - 2R)\Big)\tau \qquad \Phi_{23}^{J_2} = \kappa e^*_{xi} G(3\eta P + 4Q - 8R)\tau \tag{91}$$

$$\Phi_{24}^{J_2} = \kappa e^*_{yi} G(3\eta P + 4Q - 8R)\tau \qquad \Phi_{25}^{J_2} = 2\kappa W(-(3\eta+5)S + 2U)\cos(\Omega_i)\tau \tag{92}$$

$$\Phi_{26}^{J_2} = 2\kappa W(-(3\eta+5)S + 2U)\sin(\Omega_i)\tau \qquad \Phi_{31}^{J_2} = \frac{7}{2}\kappa e^*_{yf}(Q - 2R)\tau \tag{93}$$

$$\Phi_{33}^{J_2} = \cos((\dot{\omega}+\dot{\Omega})\tau) - 4\kappa e^*_{yf} e^*_{xi} G(Q - 2R)\tau \qquad \Phi_{34}^{J_2} = -\sin((\dot{\omega}+\dot{\Omega})\tau) - 4\kappa e^*_{yf} e^*_{yi} G(Q - 2R)\tau \tag{94}$$

$$\Phi_{35}^{J_2} = -2\kappa e^*_{yf} W(-5S + 2U)\cos(\Omega_i)\tau \qquad \Phi_{36}^{J_2} = -2\kappa e^*_{yf} W(-5S + 2U)\sin(\Omega_i)\tau \tag{95}$$

$$\Phi_{41}^{J_2} = -\frac{7}{2}\kappa e^*_{xf}(Q - 2R)\tau \qquad \Phi_{43}^{J_2} = \sin((\dot{\omega}+\dot{\Omega})\tau) + 4\kappa e^*_{xf} e^*_{xi} G(Q - 2R)\tau \tag{96}$$

$$\Phi_{44}^{J_2} = \cos((\dot{\omega}+\dot{\Omega})\tau) + 4\kappa e^*_{xf} e^*_{yi} G(Q - 2R)\tau \qquad \Phi_{45}^{J_2} = 2\kappa e^*_{xf} W(-5S + 2U)\cos(\Omega_i)\tau \tag{97}$$

$$\Phi_{46}^{J_2} = 2\kappa e_{xf}^* W(-5S+2U)\sin(\Omega_i)\tau \qquad \Phi_{51}^{J_2} = -7\kappa i_{yf}^* R\tau \qquad \Phi_{53}^{J_2} = 8\kappa e_{xi}^* i_{yf}^* GR\tau \tag{98}$$

$$\Phi_{54}^{J_2} = 8\kappa e_{yi}^* i_{yf}^* GR\tau \qquad \Phi_{55}^{J_2} = \cos(\dot{\Omega}\tau) - 4\kappa i_{yf}^* UW\cos(\Omega_i)\tau \tag{99}$$

$$\Phi_{56}^{J_2} = -\sin(\dot{\Omega}\tau) - 4\kappa i_{yf}^* UW\sin(\Omega_i)\tau \qquad \Phi_{61}^{J_2} = 7\kappa i_{xf}^* R\tau \qquad \Phi_{63}^{J_2} = -8\kappa e_{xi}^* i_{xf}^* GR\tau \tag{100}$$

$$\Phi_{64}^{J_2} = -8\kappa e_{yi}^* i_{xf}^* GR\tau \qquad \Phi_{65}^{J_2} = \sin(\dot{\Omega}\tau) + 4\kappa i_{xf}^* UW\cos(\Omega_i)\tau \tag{101}$$

$$\Phi_{66}^{J_2} = \cos(\dot{\Omega}\tau) + 4\kappa i_{xf}^* UW\sin(\Omega_i)\tau \tag{102}$$

B. Substitutions for Model-Specific STMs for Eccentric Orbits

$$\delta_1 = \frac{\partial\delta\dot{a}}{\partial\delta a}(\lambda_1 - \frac{\partial\delta\dot{e}}{\partial\delta e}) + \frac{\partial\delta\dot{e}}{\partial\delta e}(\lambda_1 - \frac{\partial\delta\dot{a}}{\partial\delta a}) + 2\frac{\partial\delta\dot{a}}{\partial\delta e}\frac{\partial\delta\dot{e}}{\partial\delta a} \qquad \delta_2 = \frac{\partial\delta\dot{a}}{\partial\delta a}(\lambda_2 - \frac{\partial\delta\dot{e}}{\partial\delta e}) + \frac{\partial\delta\dot{e}}{\partial\delta e}(\lambda_2 - \frac{\partial\delta\dot{a}}{\partial\delta a}) + 2\frac{\partial\delta\dot{a}}{\partial\delta e}\frac{\partial\delta\dot{e}}{\partial\delta a} \tag{103}$$

$$c_{111} = \frac{\frac{\partial\delta\dot{a}}{\partial\delta a}(\lambda_1 - \frac{\partial\delta\dot{e}}{\partial\delta e}) + \frac{\partial\delta\dot{a}}{\partial\delta e}\frac{\partial\delta\dot{e}}{\partial\delta a}}{\delta_1} \qquad c_{112} = \frac{\frac{\partial\delta\dot{a}}{\partial\delta a}(\lambda_2 - \frac{\partial\delta\dot{e}}{\partial\delta e}) + \frac{\partial\delta\dot{a}}{\partial\delta e}\frac{\partial\delta\dot{e}}{\partial\delta a}}{\delta_2} \qquad c_{121} = \frac{\frac{\partial\delta\dot{a}}{\partial\delta e}\lambda_1}{\delta_1} \tag{104}$$

$$c_{122} = \frac{\frac{\partial\delta\dot{a}}{\partial\delta e}\lambda_2}{\delta_2} \qquad c_{131} = \frac{\frac{\partial\delta\dot{a}}{\partial\delta B}(\lambda_1 - \frac{\partial\delta\dot{e}}{\partial\delta e}) + \frac{\partial\delta\dot{a}}{\partial\delta e}\frac{\partial\delta\dot{e}}{\partial\delta B}}{\delta_1} \qquad c_{132} = \frac{\frac{\partial\delta\dot{a}}{\partial\delta B}(\lambda_2 - \frac{\partial\delta\dot{e}}{\partial\delta e}) + \frac{\partial\delta\dot{a}}{\partial\delta e}\frac{\partial\delta\dot{e}}{\partial\delta B}}{\delta_2} \tag{105}$$

$$c_{133} = \frac{\frac{\partial\delta\dot{a}}{\partial\delta e}\frac{\partial\delta\dot{e}}{\partial\delta B} - \frac{\partial\delta\dot{a}}{\partial\delta B}\frac{\partial\delta\dot{e}}{\partial\delta e}}{\frac{\partial\delta\dot{a}}{\partial\delta a}\frac{\partial\delta\dot{e}}{\partial\delta e} - \frac{\partial\delta\dot{a}}{\partial\delta e}\frac{\partial\delta\dot{e}}{\partial\delta a}} \qquad c_{211} = \frac{\frac{\partial\delta\dot{e}}{\partial\delta a}\lambda_1}{\delta_1} \qquad c_{212} = \frac{\frac{\partial\delta\dot{e}}{\partial\delta a}\lambda_2}{\delta_2} \qquad c_{221} = \frac{\frac{\partial\delta\dot{e}}{\partial\delta e}(\lambda_1 - \frac{\partial\delta\dot{a}}{\partial\delta a}) + \frac{\partial\delta\dot{a}}{\partial\delta e}\frac{\partial\delta\dot{e}}{\partial\delta a}}{\delta_1} \tag{106}$$

$$c_{222} = \frac{\frac{\partial\delta\dot{e}}{\partial\delta e}(\lambda_2 - \frac{\partial\delta\dot{a}}{\partial\delta a}) + \frac{\partial\delta\dot{a}}{\partial\delta e}\frac{\partial\delta\dot{e}}{\partial\delta a}}{\delta_2} \qquad c_{231} = \frac{\frac{\partial\delta\dot{e}}{\partial\delta B}(\lambda_1 - \frac{\partial\delta\dot{a}}{\partial\delta a}) + \frac{\partial\delta\dot{a}}{\partial\delta B}\frac{\partial\delta\dot{e}}{\partial\delta a}}{\delta_1} \tag{107}$$

$$c_{232} = \frac{\frac{\partial\delta\dot{e}}{\partial\delta B}(\lambda_2 - \frac{\partial\delta\dot{a}}{\partial\delta a}) + \frac{\partial\delta\dot{a}}{\partial\delta B}\frac{\partial\delta\dot{e}}{\partial\delta a}}{\delta_2} \qquad c_{233} = \frac{\frac{\partial\delta\dot{a}}{\partial\delta B}\frac{\partial\delta\dot{e}}{\partial\delta a} - \frac{\partial\delta\dot{a}}{\partial\delta a}\frac{\partial\delta\dot{e}}{\partial\delta B}}{\frac{\partial\delta\dot{a}}{\partial\delta a}\frac{\partial\delta\dot{e}}{\partial\delta e} - \frac{\partial\delta\dot{a}}{\partial\delta e}\frac{\partial\delta\dot{e}}{\partial\delta a}} \tag{108}$$

C. Density-Model-Free STMs for Eccentric Orbits

$$\mathbf{\Phi}_s^{J_2+drag'}(\boldsymbol{\alpha}_c(t_i),\tau) = \left[\begin{array}{c:c} \mathbf{\Phi}_s^{J_2}(\boldsymbol{\alpha}_c(t_i),\tau) & \begin{array}{c}\tau\\ (-\frac{3}{4}n - \frac{7}{4}\kappa\eta P + \frac{3}{2}\kappa e(1-e)\eta GP)\tau^2\\ (1-e)\tau\\ \kappa Q(-\frac{7}{4} + 2e(1-e)G)\tau^2\\ 0\\ \kappa R(\frac{7}{2} - 4e(1-e)G)\tau^2\end{array} \\ \hdashline \mathbf{0}^{1\times 6} & 1 \end{array}\right] \tag{109}$$

$$\mathbf{\Phi}_{qns}^{J_2+drag'}(\boldsymbol{\alpha}_c(t_i),\tau) = \left[\begin{array}{c:c} \mathbf{\Phi}_{qns}^{J_2}(\boldsymbol{\alpha}_c(t_i),\tau) & \begin{array}{c}\tau\\ (-\frac{3}{4}n - \frac{7}{4}\kappa EP + \frac{1}{2}\kappa e(1-e)FGP)\tau^2\\ (1-e)\cos(\omega_f)\tau - \kappa e_{yf}Q(-\frac{7}{4} + 2e(1-e)G)\tau^2\\ (1-e)\sin(\omega_f)\tau + \kappa e_{xf}Q(-\frac{7}{4} + 2e(1-e)G)\tau^2\\ 0\\ \kappa S(\frac{7}{4} - 2e(1-e)G)\tau^2\end{array} \\ \hdashline \mathbf{0}^{1\times 6} & 1 \end{array}\right] \tag{110}$$

$$\mathbf{\Phi}_{ns}^{J_2+drag'}(\boldsymbol{\alpha}_c(t_i),\tau) = \left[\begin{array}{c:c} \mathbf{\Phi}_{ns}^{J_2}(\boldsymbol{\alpha}_c(t_i),\tau) & \begin{array}{c}\tau\\ (-\frac{3}{4}n - \frac{7}{4}\kappa(\eta P + Q - 2R) + \frac{1}{2}\kappa e(1-e)G(3\eta P + 4Q - 8R))\tau^2\\ (1-e)\cos(\omega_f + \Omega_f)\tau - \kappa e_{yf}^*(Q-2R)(-\frac{7}{4} + 2e(1-e)G)\tau^2\\ (1-e)\sin(\omega_f + \Omega_f)\tau + \kappa e_{xf}^*(Q-2R)(-\frac{7}{4} + 2e(1-e)G)\tau^2\\ -\kappa i_{yf}^* R(\frac{7}{2} - 4e(1-e)G)\tau^2\\ \kappa i_{xf}^* R(\frac{7}{2} - 4e(1-e)G)\tau^2\end{array} \\ \hdashline \mathbf{0}^{1\times 6} & 1 \end{array}\right] \tag{111}$$

D. Density-Model-Free STMs for Orbits of Arbitrary Eccentricity

$$\boldsymbol{\Phi}_s^{J_2+drag*}(\boldsymbol{\alpha}_c(t_i),\tau) = \left[\begin{array}{c:ccc} \boldsymbol{\Phi}_s^{J_2}(\boldsymbol{\alpha}_c(t_i),\tau) & \tau & 0 & 0 \\ & -(\frac{3}{4}n+\frac{7}{4}\kappa\eta P)\tau^2 & \frac{3}{2}\kappa e\eta GP\tau^2 & -\tau \\ & 0 & \tau & 0 \\ & -\frac{7}{4}\kappa Q\tau^2 & 2\kappa eGQ\tau^2 & \tau \\ & 0 & 0 & 0 \\ & \frac{7}{2}\kappa R\tau^2 & -4\kappa eGR\tau^2 & 0 \\ \hdashline \mathbf{0}^{3\times 6} & \multicolumn{3}{c}{\mathbf{I}^{3\times 3}} \end{array}\right] \tag{112}$$

$$\boldsymbol{\Phi}_{qns}^{J_2+drag*}(\boldsymbol{\alpha}_c(t_i),\tau) = \left[\begin{array}{c:ccc} \boldsymbol{\Phi}_{qns}^{J_2}(\boldsymbol{\alpha}_c(t_i),\tau) & \tau & 0 & 0 \\ & -(\frac{3}{4}n+\frac{7}{4}\kappa EP)\tau^2 & \frac{1}{2}\kappa eFGP\tau^2 & 0 \\ & \frac{7}{4}\kappa e_{yf}Q\tau^2 & \cos(\omega_f)\tau - 2\kappa ee_{yf}GQ\tau^2 & -\sin(\omega_f)\tau \\ & -\frac{7}{4}\kappa e_{xf}Q\tau^2 & \sin(\omega_f)\tau + 2\kappa ee_{xf}GQ\tau^2 & \cos(\omega_f)\tau \\ & 0 & 0 & 0 \\ & \frac{7}{4}\kappa S\tau^2 & -2\kappa eGS\tau^2 & 0 \\ \hdashline \mathbf{0}^{3\times 6} & \multicolumn{3}{c}{\mathbf{I}^{3\times 3}} \end{array}\right] \tag{113}$$

$$\boldsymbol{\Phi}_{ns}^{J_2+drag*}(\boldsymbol{\alpha}_c(t_i),\tau) =$$

$$\left[\begin{array}{c:ccc} \boldsymbol{\Phi}_{ns}^{J_2}(\boldsymbol{\alpha}_c(t_i),\tau) & \tau & 0 & 0 \\ & -(\frac{3}{4}n+\frac{7}{4}\kappa(\eta P+Q-2R))\tau^2 & \frac{1}{2}\kappa eG(3\eta P+4Q-8R)\tau^2 & 0 \\ & \frac{7}{4}\kappa e_{yf}^*(Q-2R)\tau^2 & \cos(\omega_f+\Omega_f)\tau - 2\kappa ee_{yf}^*G(Q-2R)\tau^2 & -\sin(\omega_f+\Omega_f)\tau \\ & -\frac{7}{4}\kappa e_{xf}^*(Q-2R)\tau^2 & \sin(\omega_f+\Omega_f)\tau + 2\kappa ee_{xf}^*G(Q-2R)\tau^2 & \cos(\omega_f+\Omega_f)\tau \\ & -\frac{7}{2}\kappa i_{yf}^*R\tau^2 & 4\kappa ei_{yf}^*GR\tau^2 & 0 \\ & \frac{7}{2}\kappa i_{xf}^*R\tau^2 & -4\kappa ei_{xf}^*GR\tau^2 & 0 \\ \hdashline \mathbf{0}^{3\times 6} & \multicolumn{3}{c}{\mathbf{I}^{3\times 3}} \end{array}\right] \tag{114}$$